A descending pathway facilitates undulatory wave propagation in *Caenorhabditis elegans* through gap junctions

Tianqi Xu[1,3], Jing Huo[1,3], Shuai Shao[1], Michelle Po[2], Taizo Kawano[2], Yangning Lu[2], Min Wu[2], Mei Zhen[2], Quan Wen[1,*]

1. Chinese Academy of Sciences Key Laboratory of Brain Function and Disease, School of Life Sciences, Center for Excellence in Brain Science and Intelligence Technology, University of Science and Technology of China, Hefei, 230027, China

2. Lunenfeld-Tanenbaum Research Institute, Mount Sinai Hospital; Department of Molecular Genetics, Department of Physiology, University of Toronto, Toronto, ON, Canada, M5G 1X5

3. These authors contributed equally to this work

*Corresponding author: qwen@ustc.edu.cn

Descending signals from the brain play critical roles in controlling and modulating locomotion kinematics. In the *Caenorhabditis elegans* nervous system, descending AVB premotor interneurons exclusively form gap junctions with B-type motor neurons that drive forward locomotion. We combined genetic analysis, optogenetic manipulation, and computational modeling to elucidate the function of AVB-B gap junctions during forward locomotion. First, we found that some B-type motor neurons generated intrinsic rhythmic activity, constituting distributed central pattern generators. Second, AVB premotor interneurons drove bifurcation of B-type motor neuron dynamics, triggering their transition from stationary to oscillatory activity. Third, proprioceptive couplings between neighboring B-type motor neurons entrained the frequency of body oscillators, forcing coherent propagation of bending waves. Despite substantial anatomical differences between the worm motor circuit and those in higher model organisms, we uncovered converging computational principles that govern coordinated locomotion.

Key words: Descending pathway; motor control; central pattern generator (CPG); *C. elegans*; optogenetics; proprioception; gap junction

Introduction

Locomotion requires coordinated rhythmic motor activity. In vertebrate and invertebrate motor systems, oscillatory signals that innervate muscles are generated by dedicated neurons and neural circuits with intrinsic rhythmic properties, called central pattern generators (CPGs) [1-6]. Movements, which constitute muscle activities of defined spatial pattern and temporal sequence, are driven by CPG modules distributed at different body segments. Coordination of rhythmic movements requires coupling mechanisms, by which the rhythm of multiple CPGs becomes frequency- and phase-locked [5, 7].

Although the activity of CPGs is intrinsic and independent of sensory inputs, proprioceptive or mechanosensitive feedback reshapes the motor dynamics during movement [8]. In lamprey and leech, for example, activation of specialized proprioceptive neurons, either by current injection or externally imposed body bending, entrains the motor CPG activity [9, 10]. In limbed animals, rapid phasic feedback from mechanoreceptors tunes the rhythmic firing of motor neurons during step cycles [11-13]. Mice lacking Piezo2, a mechanically activated channel expressed in proprioceptive neurons, exhibit severely uncoordinated body movement [14].

Descending signals, typically the projections of glutamatergic neurons from the brain to the spinal or nerve cords, regulate both CPG activity and motor patterns [15]. In fish and rodent, descending reticulospinal neurons, arising from the brainstem and innervating excitatory spinal interneurons, can initiate locomotion and modulate speed [16-19]; whereas those that activate inhibitory spinal interneurons can terminate locomotion [20]. Descending interneurons that directly target the forelimb motor neurons are critical for skillful motor behaviors [21]. In leech, activation of a descending command interneuron, cell 204, can initiate and maintain swimming behavior [7, 22].

A deep understanding of the motor circuit must integrate local CPG elements and sensory feedback, as well as global command signals, to predict behavioral dynamics from interaction of individual circuit components [23, 24]. With a connectome at synaptic

resolution and fully identified cell-types [25, 26], *Caenorhabditis elegans* offers an opportunity to obtain a complete, system-level understanding of a locomotor circuit.

The *C. elegans* ventral nerve cord consists of a network of excitatory cholinergic motor neurons, the A- and B-type that drive backward and forward movement, respectively, and the inhibitory motor neurons (D-type) that are innervated by the excitatory motor neurons [27]. The AVB premotor interneurons, which receive numerous inputs from sensory and other interneurons, extend long processes along the entire ventral nerve cord, and exclusively form gap junctions with the B-type motor neurons [26, 28, 29] (Figure 1a). The functions of AVB premotor interneurons and their electrical synapses with B-type motor neurons, however, are poorly understood.

Here, we took an integrative approach to defining the circuit logic underlying coordinated locomotion in *C. elegans*, with an emphasis on how descending signals modulate the dynamics of the motor circuit. Whereas descending inputs in other systems directly drive or modulate the activity of locomotor CPGs [16-18], it remains unclear whether similar CPG elements exist in *C. elegans*. Combining molecular genetics and optical manipulation of neuronal activity in freely behaving *C. elegans*, we found that mid-body B-type motor neurons could function as oscillators. To generate coherent body undulation, the intrinsic activity in B-type motor neurons was entrained by proprioceptive feedback. To promote forward movement, AVB-B gap junctions drove the bifurcation of B-type neuron dynamics from stationary to rhythmic activity.

Previously, we demonstrated the proprioceptive properties in B-type motor neurons: directional proprioceptive couplings between B-type motor neurons are responsible for the propagation of rhythmic head bending along the body [30, 31]. Our current experimental and computational analyses suggest that descending signals from the AVB premotor interneurons function synergistically with proprioceptive couplings to facilitate sequential activation of motor neuron activities, allowing body bending to propagate directionally and efficiently to drive forward locomotion.

Results

Gap junctions between descending AVB premotor interneurons and B-type motor neurons facilitate bending wave propagation during forward locomotion

The AVB premotor interneurons and B-type motor neurons form heterotypic gap junctions via the UNC-7 innexin (in AVB) and UNC-9 innexin (in B-type) (Figure 1a) [28, 29]. To determine whether AVB-B gap junctions play a role in forward locomotion, we first examined the motor behaviors of *unc-7*(*hp121*) and *unc-9*(*fc16*) null mutants immersed in viscous solution (1 Pa·s viscosity). In these gap junction-deficient mutants, the intrinsically higher levels of activity in the A-type motor neurons, which control backward locomotion, prevent animals from generating continuous forward movement [29]. To reduce interference from motor activity arising from the backward motor circuit, A-type motor neurons were constitutively silenced by an active K^+ channel [P*unc-4*::TWK-18(gf)] in examined strains and experiments (Supplementary Table).

We visualized and quantified *C. elegans* locomotion kinematics by curvature kymographs (Figure 1b). During bouts of forward movement, each body segment alternated between positive (red) and negative (blue) curvature, and the stripes of curvature propagated from the head to the tail. Coordinates along the worm body were defined as head = 0 and tail = 1 (Figure 1b). In control animals (wild-type with A-type motor neurons constitutively silenced), the bending amplitude was highest near the head, then declined gradually and plateaued at the mid-body (~ 40% of the body length, Figure 1c). Both *unc-7* and *unc-9* mutants exhibited identical phenotypes: their bending amplitudes diminished monotonically towards the tail (Figure 1b–d and Video 1).

UNC-7 and UNC-9 are involved in gap junction couplings in many neurons besides AVB and B-type neurons [28, 32]. We next showed that disruption of AVB-B gap junctions was responsible for the monotonic decline of bending amplitudes in *unc-7* and *unc-9* mutants. First, when AVB premotor interneurons were optogenetically ablated using miniSOG [33] (by either P*lgc-55(B)*::miniSOG or P*sra-11*::miniSOG), we observed the

same trend of bending amplitude decline towards the tail (Figure 1b-d and Figure 1 - figure supplement 1). Second, restoring innexin UNC-7 in the AVB interneurons (*unc*-7; P*sra-11*::UNC-7) in *unc-7* mutants was sufficient to restore the plateau phase of bending amplitude (Figure 1c-d and Video 3).

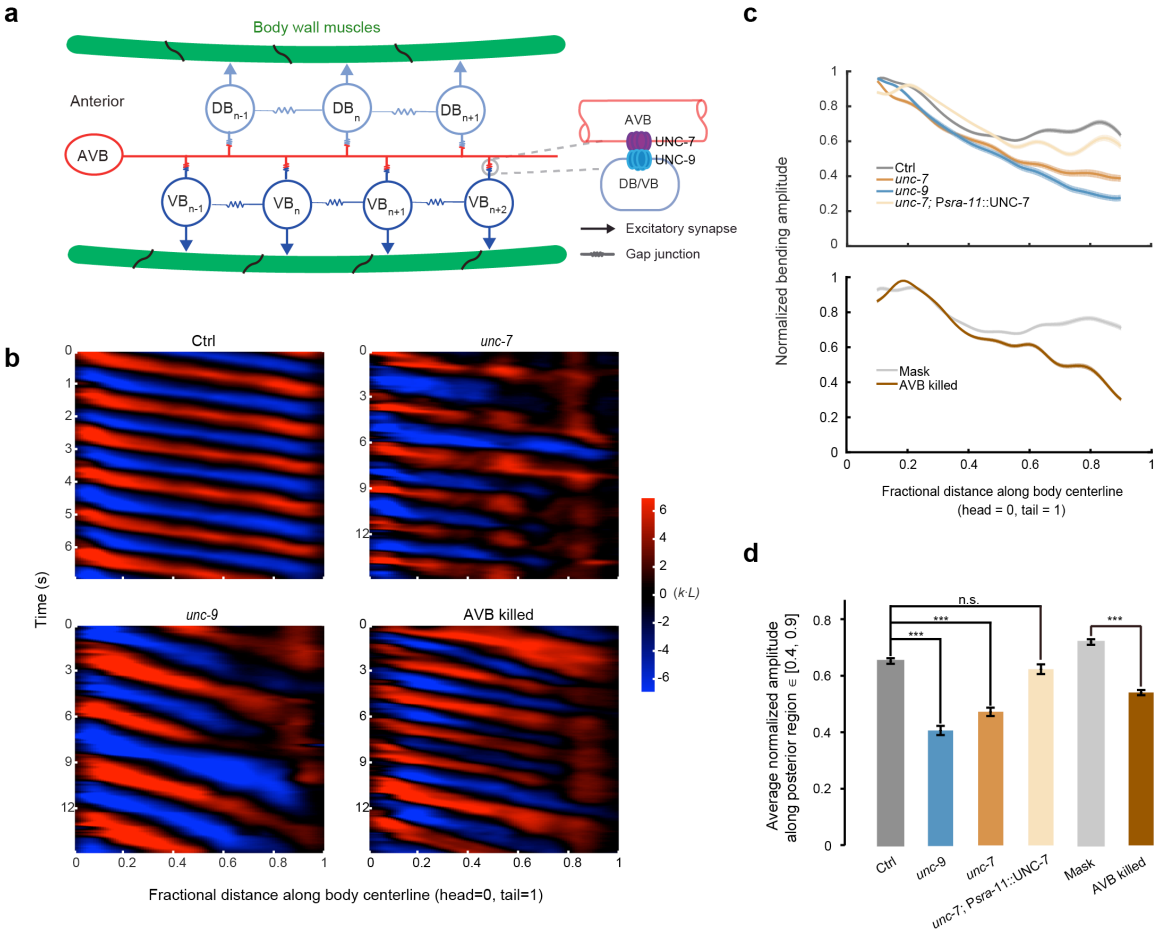

Figure 1. AVB-B gap junctions facilitate undulatory wave propagation during forward locomotion **(a)** Schematics of gap junction couplings in the *C. elegans* forward motor circuit. The AVB premotor interneurons form gap junctions with all B-type motor neurons, which drive dorsal (DB) and ventral (VB) muscle contraction. AVB-B gap junctions require the expression of innexin UNC-7 in AVB interneurons and UNC-9 in B-type motor neurons. Neighboring B-type neurons are also gap junction coupled. Other types of motor neurons have been omitted from the diagram for simplicity. **(b)** Representative curvature kymographs of control (N2; P*unc-4*::TWK-18(gf)), *unc-7* (*unc-7*(*hp121*); P*unc-4*::TWK-18(gf)), *unc-9* (*unc-9*(*fc16*); P*unc-4*::TWK-18(gf)) animals, and AVB-ablated (P*lgc-55*::miniSOG; P*unc*-4::TWK-18(gf)) and their control (Mask-ablated) animals. Worms swam in viscous solutions (~ 1 Pa·s viscosity). Body curvature was defined as a non-dimensional unit $k{\cdot}L$, where L is the body length. **(c)** Quantification of the bending amplitude along the body for strains described above. Shaded regions represent s.e.m. Amplitude

was normalized against the maximum curvature along the body. **(d)** Averaged bending amplitude in the posterior body ∈ [40, 90] for strains described above. *** $p < 0.0001$ (Ctrl and *unc-9* $p = 3.5\times10^{-23}$; Ctrl and *unc-7* $p = 1.9\times10^{-20}$; Mask and AVB killed $p = 3.0\times10^{-28}$), two-sample *t*-test with Bonferroni correction, n.s. $p = 0.16$. Error bars represent s.e.m. Ctrl, $n = 105$ independent measurements, 13 worms; *unc-7* mutant, $n = 149$ measurements, 22 worms; *unc-9* mutant, $n = 93$ measurements, 17 worms; AVB-ablated, $n = 80$ measurements, 13 worms; Mask (same genotype without ablation), $n = 96$ measurements, 12 worms.

Linear proprioceptive coupling model predicts deteriorated undulatory waves in the presence of AVB-B gap junctions

We next asked why AVB-B gap junction-deficient worms could not efficiently propagate body bending towards the tail. Previously, we showed that worm undulation during forward locomotion requires proprioceptive coupling between adjacent body regions [30]. Curvature change in a mid-body region, induced by a pneumatic microfluidic device, activates bend-sensitive B-type neurons and defines the curvature of the posterior neighbor [30]. Consistently, when we trapped the middle body region of a wild-type worm in a static channel with defined curvature, the unrestrained posterior body region exhibited bending curvature in the same direction as that imposed by the microfluidic channel (Figure 2a-b and [30]).

To determine whether the proprioceptive coupling is UNC-7- and UNC-9-dependent, we examined *unc-7* and *unc-9* mutants constrained by microfluidic channels. Consistent with a previous finding [30] and observation from control animals, their posterior body regions still followed the curvature imposed on the anterior body regions (Figure 2b-c and Figure 2 - figure supplement 1). Therefore, proprioceptive coupling remains largely intact in the absence of UNC-7- or UNC-9-dependent gap junctions.

We next took a theoretic approach to probing how AVB-B gap junctions might affect bending wave propagation. We first adopted a linear proprioceptive coupling model [30], where we asserted that the undulatory wave started with rhythmic dorsal/ventral bends near the head (Methods). Directional proprioceptive coupling between adjacent body regions is fully described by a set of first order differential equations:

$$\begin{cases} C_m \dfrac{dv_i}{dt} = g_m(-v_i + ck_{i-1}) - g(v_i - v_{AVB}), \\ \tau_h \dfrac{du_i}{dt} = -u_i + v_i, \\ \tau_\eta \dfrac{dk_i}{dt} = -k_i + \alpha_{max} * u_i/b\,. \end{cases} \qquad i = 2,3,\ldots 6 \quad \text{(Equation 1)}$$

We divided the whole worm into several segments, with subscript i as the segment number. In the first equation, v describes relative motor neuron activity: when dorsal B-type neurons have a higher activity than ventral ones, $v > 0$, and vice versa. k_i is the curvature of a given segment, and ck_{i-1} describes the proprioceptive signal from the neighboring anterior body segment, where $c > 0$ is the coupling strength. C_m is the membrane capacitance and g_m is the leaky conductance. The term $-g(v_i - v_{AVB})$ describes the contribution from AVB-B electrical coupling, where g is the gap junction conductance. For simplicity, we set $v_{AVB} = 0$ to eliminate the bias of v. A more detailed model that treated dorsal and ventral motor neuron activities separately is described in the Methods.

The second equation relates motor neuron activity to muscle torque: u is a dimensionless variable and $\alpha_{max} * u$ is the maximum torque that the muscle cells can generate. The last equation describes how the segment curvature changes with muscle torque: b is the bending modulus of the body and τ_η is a time constant [30] proportional to the viscosity η of the medium.

Simulation of the linear coupling model predicted an exponential decay of bending amplitude towards the tail (Figure 2d). By transforming Equation 1 into a continuous form (see Methods), we solved this linear model analytically and identified a self-consistent solution for the spatiotemporal profile of the worm body curvature:

$$k(x,t) = k_0 \exp(-x/\xi) \exp\left(i\left(\frac{2\pi x}{\lambda} - \omega t + \phi(x)\right)\right), \qquad \text{(Equation 2)}$$

where ω and λ describe the angular frequency and spatial wavelength of undulation, respectively; $\phi(x)$ is a phase lag term, and ξ is the decay length constant, which, to the leading order, is given by:

$$\xi \approx \frac{l}{1 - c\alpha_{max}/b}, \qquad \text{subject to } \frac{c\alpha_{max}}{b} \leq 1 \qquad \text{(Equation 3)}$$

where l is the spatial scale for proprioceptive coupling [30]. $\xi \to +\infty$ leads to identical bending amplitude along the body. Incorporation of AVB-B electrical coupling effectively changes c to $cg_m/(g_m + g)$. This prefactor further reduces the length constant. In a linear coupling model where B-type motor neurons are passive recipients of proprioceptive inputs, opposite to our experimental findings, gap junctions between AVB and B-type neurons would deteriorate the propagation of bending waves (Figure 2d).

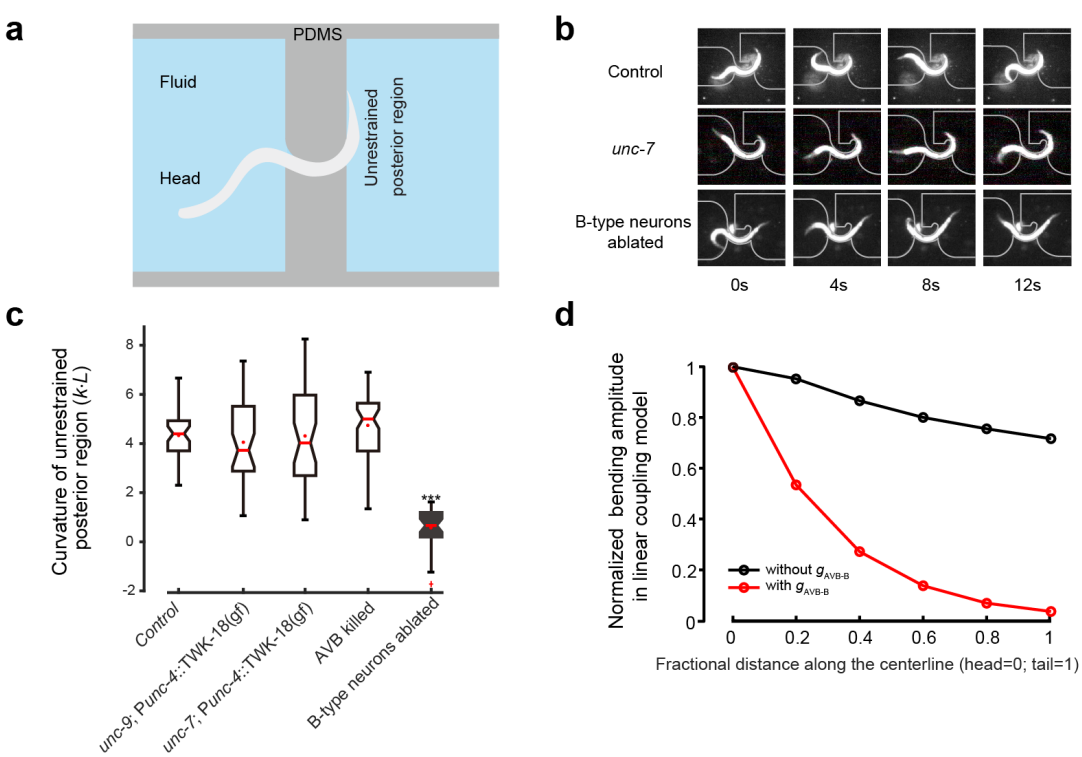

Figure 2. UNC-7- and UNC-9-dependent gap junctions are not required for proprioceptive couplings in the forward motor circuit. (a) Schematics of the microfluidic device for constraining a body segment with defined curvature. **(b)** Time-lapse video images of control (upper panel), *unc-7* (middle panel), and B-type neuron-ablated (lower panel) worms trapped in the microfluidic device. In both control and *unc-7* mutant animals, the posterior unrestrained body region followed the curvature of the channel. However, this was not the case when B-type motor neurons were optogenetically ablated. **(c)** In AVB-B gap junction-deficient mutants, or AVB-ablated worms, the posterior unrestrained body region also followed the curvature of the channel. Boxes indicate Q1 to Q3, error bars represent Q1-1.5IQR and Q3+1.5IQR respectively, notches indicate 95% confidence interval. *** $p < 0.0001$ ($p = 1.3\times10^{-6}$) , compared with other strains, by Mann-Whitney U test. Control; (N2; P*unc-4*::TWK-18(*gf*)), n = 40 measurements, 8 worms; *unc-7* (*unc-7;* P*unc-4*::TWK-18(gf)), n = 41 measurements, 12 worms; *unc-9* (*unc-9;* P*unc-4*::TWK-18(gf)), n = 38 measurements, 9 worms; AVB-ablated (P*lgc-55(B)*::miniSOG), n = 60 measurements, 10 worms; B-ablated (P*acr-5*::miniSOG), n = 33 measurements, 9 worms. **(d)** In the linear proprioceptive coupling model, incorporating the AVB-B gap junction inputs further deteriorated bending wave propagation.

B-type motor neurons are nonlinear functional units

The discrepancy between the theoretical model and experimental observations indicates that some basic assumption in the linear model must be modified. We hypothesized that proprioceptive signals couple nonlinear functional units within adjacent regions. Intrinsic oscillation is a common form of nonlinearity. We thus tested whether CPGs exist along the worm nerve cord.

Our linear coupling model predicted that abolishing head bending activity would abolish the undulatory wave; a coupled-CPG model, however, predicts the opposite. To distinguish these possibilities, we performed spatially selective optogenetic inhibition of B-type motor neurons in a defined anterior body region (0.1–0.3 along worm coordinates) of a freely swimming animal (P*acr-5*::Arch) (Figure 3a–b and Video 2). Upon green light illumination, we effectively abolished bending near the head region (Figure 3b, curvature kymograph). The mid-body (~ 50% of the body length), however, continued to generate rhythmic bending with increased undulation frequency and reduced amplitude (Figure 3b, 3e, Video 2). When a worm swam in 1 Pa·s viscous solution, the undulation frequency was ~ 0.8 Hz (Figure 3c); when anterior bending activity was optogenetically inhibited,

the mid-body undulation frequency doubled (~ 1.6 Hz, Figure 3c). We observed a similar phenomenon when anterior undulation was abolished optogenetically, either by inhibiting both A-type and B-type motor neurons (P*acr-2*::Arch, Figure 3 - figure supplement 1a), or by directly inhibiting anterior muscle cells (P*myo-3*::NpHR, Figure 3 - figure supplement 1a).

These observations favor the possibility that at least some B-type motor neurons are intrinsic oscillators. Whereas the normal undulation frequency decreased in more viscous solution (Figure 3c and [34]), the mid-body undulation frequency remained fixed across a wide range of viscosities when anterior bending activity was abolished (Figure 3c and Figure 3 - figure supplement 1b). Therefore, the intrinsic frequency of the mid-body oscillators, which could be entrained by head bending, appeared to be independent of the mechanical load of the environment.

To determine whether the B-type motor neurons were responsible for generating intrinsic mid-body oscillation, we performed systematic ablation of B-type neurons (P*acr-5*::miniSOG) in the ventral nerve cord. Ablating a cluster of mid-body B-type motor neurons (DB4-5 and VB5-7) abolished high-frequency oscillation when anterior bending activity was abolished (Figure 3d-e). When only a subset of neurons in this cluster was ablated, the high-frequency mid-body undulation could still be induced (Figure 3 - figure supplement 1a). In these animals, we occasionally observed independent bending waves generated by the head and posterior body regions, respectively (Figure 3 - figure supplement 1c). We also confirmed that D-type inhibitory motor neurons were not involved in generating intrinsic mid-body undulation (Figure 3 - figure supplement 1a). Together, these data strongly suggest that B-type motor neurons do not passively respond to proprioceptive signals from the anterior segment. They instead function as nonlinear units that resemble distributed CPG modules along the body.

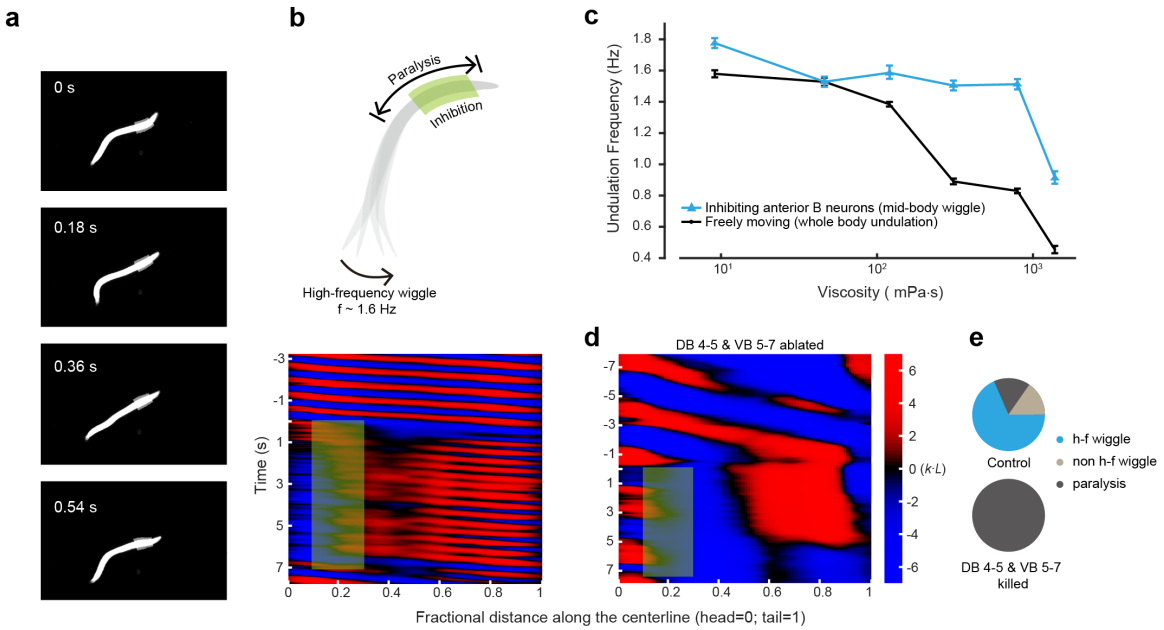

Figure 3 Mid-body B-type motor neurons generate rhythmic activity independent of proprioceptive coupling. (a) Time-lapse video images from a recording when B-type motor neurons in an anterior body region (10–30% along the worm body) were optogenetically inhibited. **(b)** Upper panel, schematic illustrates the effect of spatially selective inhibition of B-type motor neurons. Optogenetic inhibition of anterior B-type motor neurons induced high-frequency undulation in the posterior region; lower panel, representative curvature kymograph. Green shaded region shows the selected spatiotemporal region for optogenetic inhibition. **(c)** *C. elegans* undulation frequency at different viscosity. Black line is undulation frequency of control animals; blue line is mid-body undulation frequency when anterior bending activity was abolished. Error bars are s.e.m.; $n \geq 8$ worms for each data point. **(d)** Representative curvature kymograph during optogenetic inhibition of anterior B-type motor neurons, with and without mid-body B-type neurons (DB 4–5 & VB 5–7). **(e)** Pie chart summarizes the percentage of locomotor states when anterior bending activity was abolished. h-f wiggle: mid-body undulation frequency was higher than that before anterior bending activity was abolished; non-h-f wiggle: mid-body undulation frequency was equal to or less than that before anterior bending activity was abolished; paralysis: no waves emerged in the mid-body. Control (P*acr-5*::Arch), n = 241 measurements, 20 worms; Mid-body B-type neuron-ablated worms (P*acr-5*::Arch; P*acr-5*::miniSOG), n = 77 measurements, 11 worms.

AVB-B gap junctions drive the bifurcation of B-type motor neuron dynamics

We next asked whether AVB-B gap junction inputs played a role in high-frequency mid-body undulation when anterior bending activity was abolished. Indeed, in AVB-B gap junction-deficient mutants (*unc-7* and *unc-9*), as well as AVB-ablated animals, optogenetic inhibition of anterior bending no longer induced mid-body undulation (Figure 4a-b). Instead, optogenetic inhibition of either anterior B-type motor neurons or anterior body wall muscles led to paralysis of the whole-body (Figure 4a-b and Figure 4 - figure supplement 1). Restoring UNC-7 innexin expression in AVB interneurons (*unc*-7; P*sra-11*::UNC-7; P*unc-4*:TWK-18(gf)) significantly increased the efficacy for inducing high frequency mid-body undulation (Figure 4b and Video 3). These results strongly suggest that AVB interneurons and their gap junction couplings with B-type motor neurons are required for inducing mid-body high frequency undulation. Consistently, optogenetic activation of the AVB interneurons (*Psra-11*::Chrimson) reliably triggered forward locomotion from either the pause state or the backward movement (Figure 4c, Video 7).

AVB interneurons exhibit elevated yet *non-oscillatory* calcium activity during forward locomotion [29, 35, 36]. Our data thus suggest that AVB-B gap junctions drive a bifurcation of B-type neuron dynamics, leading to a transition from the stationary to oscillatory state. In the presence of AVB-B gap junctions, time-varying proprioceptive signals from the anterior body may easily induce changes in motor neuron membrane potential, thus facilitating bending wave propagation.

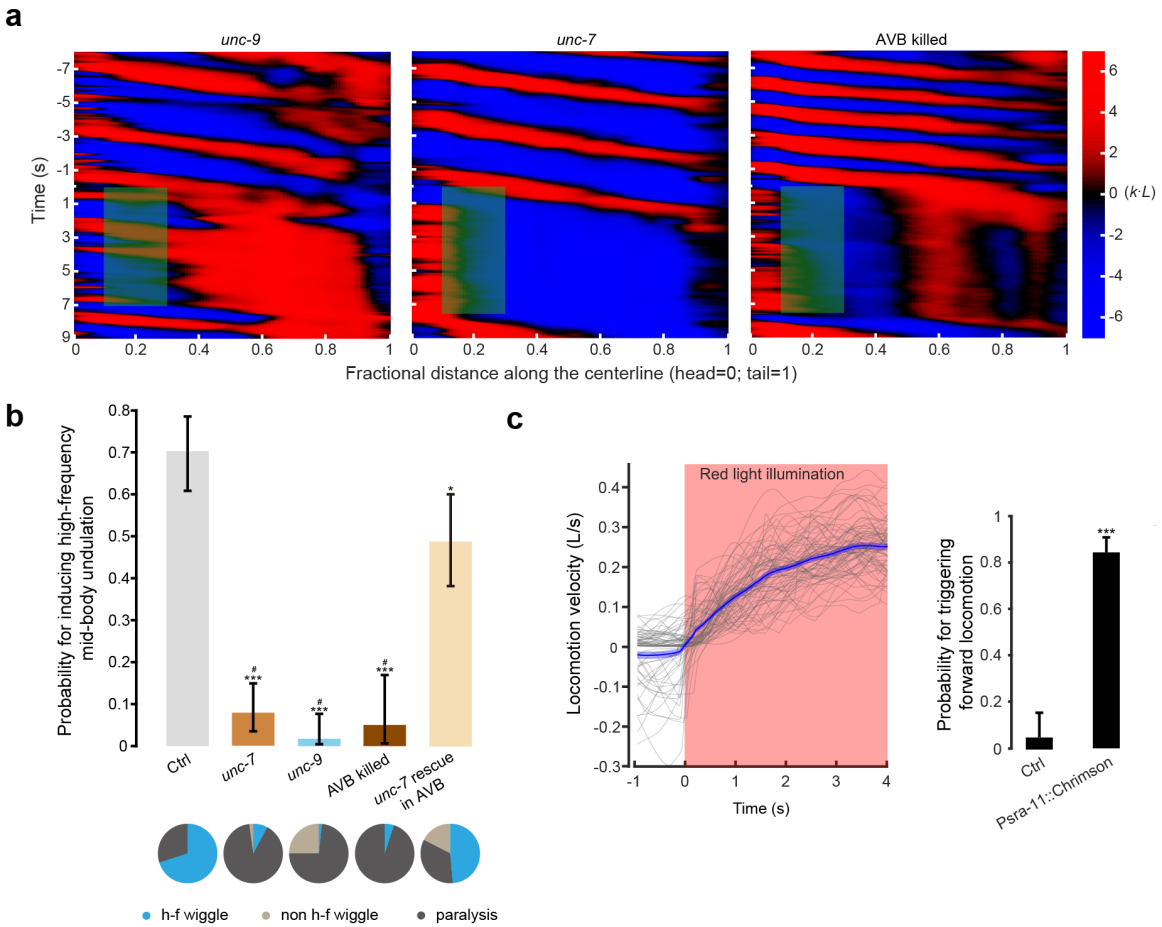

Figure 4. AVB-B electrical coupling drives the bifurcation in the B-type neuron dynamics. (a) Representative curvature kymographs in AVB-B gap junction-deficient or AVB-ablated worms when anterior bending activity was abolished. **(b)** Probability for inducing high-frequency mid-body undulation when anterior bending activity was abolished. Pie chart summarizes the percentage of worm locomotor states. Error bars indicate 95% binomial proportion confidence interval. *** $p < 0.0001$, * $p = 0.002$, # $p < 0.0001$ (* compared with Ctrl, # compared with UNC-7 rescued in AVB. Ctrl and *unc-7* $p = 1.8\times10^{-20}$; Ctrl and *unc-9* $p = 1.4\times10^{-26}$; Ctrl and AVB killed $p = 5.0\times10^{-12}$; Ctrl and *unc-7* rescue in AVB $p = 0.002$; *unc-7* rescue in AVB and *unc-7* $p = 2.3\times10^{-10}$; *unc-7* rescue in AVB and *unc-9* $p = 4.2\times10^{-15}$; *unc-7* rescue in AVB and AVB killed $p = 4.1\times10^{-6}$) Chi-square test. Strains for comparisons are: control [P*acr-5*::Arch; P*unc-4*::TWK-18(gf)], n = 113 measurements, 13 worms; *unc-7* [*unc-7*(*hp121*); P*acr-5*::Arch; P*unc-4*::TWK-18(gf)] n = 102 measurements, 21 worms; *unc-9* [*unc-9*(*fc16*); P*acr-5*::Arch; P*unc-4*::TWK-18(gf)] n = 116 measurements, 26 worms; AVB-ablated [P*lgc-55(B)*::miniSOG, P*acr-5*::Arch] n = 40 measurements, 11 worms; UNC-7 rescued in AVB [*unc-7*(*hp121*); P*acr-5*::Arch; P*unc-4*::TWK-18(gf); P*sra-11*::UNC-7] n = 86 measurements, 12 worms. **(c)** Optogenetic activation of AVB premotor interneurons could trigger forward locomotion. Left panel, optogenetic activation (P*sra*-11::Chrimson, n = 133 measurements, 11 worms), showing locomotion velocity with time, red light (635 nm, 12 mW/mm^2) was turned on at t = 0. Gray traces represent individual trials, and shaded region represents s.e.m. Right,

probability for triggering forward locomotion. Ctrl represents worms without feeding all-*trans* retinal. Error bars indicate 95% binomial proportion confidence interval, ***$p < 0.0001$ ($p = 2.6\times10^{-7}$), Chi-square test.

Nonlinear proprioceptive coupling model recapitulates AVB-B gap junction-dependent bifurcation of B-type motor neuron dynamics

We next sought theoretical verification of our functional model. For simplicity, we developed a phenomenological model based on active Ca^{2+} and K^{+} conductance [37], in which the dynamics of dorsal and ventral motor neurons within a given body segment are governed by the following equations:

$$\begin{cases} C_m \dfrac{dV_{di}}{dt} = -g_L(V_{di} - E_L) - g_{Ca} m_\infty(V_{di}) * (V_{di} - E_{Ca}) - g_K n_d * (V_{di} - E_K) + c' k_{i-1} + g(V_{AVB} - V_{di}) \\ \tau_n \dfrac{dn_d}{dt} = -n_d + n_\infty(V_{di}) \\ C_m \dfrac{dV_{vi}}{dt} = -g_L(V_{vi} - E_L) - g_{Ca} m_\infty(V_{vi}) * (V_{vi} - E_{Ca}) - g_K n_v * (V_{vi} - E_K) - c' k_{i-1} + g(V_{AVB} - V_{vi}) \\ \tau_n \dfrac{dn_v}{dt} = -n_v + n_\infty(V_{vi}) \end{cases}$$

(Equation 4)

In Equation 4, V is motor neuron membrane potential; subscripts $d\ and\ v$ denote dorsal and ventral sides, respectively; m and n are voltage-dependent Ca^{2+} and K^{+} activation variables, respectively. Parameter values in this equation were chosen (Methods) to accommodate the following experimental findings. First, when the head and body undulations were decoupled ($c'k_1 \approx 0$), gap junctions between AVB interneurons and B-type motor neurons induced high frequency motor neuron oscillation (Figure 5a). Second, proprioceptive signals arising from head bending entrained posterior motor neuron oscillation (Figure 5a). The nullcline analysis, which allows for visualization of the dynamical variables on a vector field, provided useful information on the transition from the resting state to the limit cycle in the presence of AVB-B gap junctions (Figure 5b). Furthermore, simulation recapitulated the experimental finding that AVB-B gap junctions helped equalize bending amplitude along the body (Figure 5c).

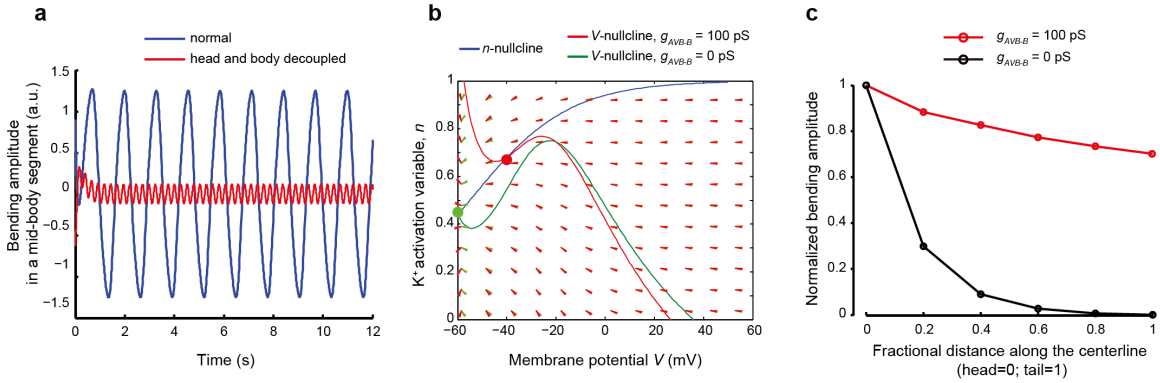

Figure 5. Simulation of a nonlinear proprioceptive coupling model. (a) Bending activity of a mid-body segment. Blue, bending amplitude during normal locomotion; red, when the head and body undulation was decoupled, oscillation with higher frequency and lower amplitude emerged. **(b)** Nullcline analysis of motor neuron dynamics. The *n*- and *V*-nullclines were defined as $\frac{dn}{dt} = 0, \frac{dV}{dt} = 0$, respectively. In the absence of proprioceptive coupling and AVB-B gap junctions ($g_{AVB-B} = 0$), the fixed point of the membrane potential dynamics (green) corresponds to a steady state; in the presence of AVB-B gap junctions, that is, $g_{AVB-B} = 100\,ps$, the system undergoes bifurcation, and the new fixed point becomes unstable (red), leading to periodic oscillation. **(c)** A comparison of bending amplitude along the body, with and without AVB-B gap junctions. All parameters used in the simulation are described in the Methods.

Electrical couplings between motor neurons and AVB-B gap junctions permit rapid and reciprocal interactions between head and body motor activities

Having considered the functions of the AVB-B gap junctions, we next asked whether local gap junctions between B-type motor neurons (Figure 1a), identified by anatomical wiring [25, 26], played additional roles in forward locomotion.

This question arises from our observation that inhibition of B-type motor neurons in middle or posterior body regions, unlike the anterior body region, induced rapid (within ~ 300 ms) paralysis of the whole worm (Figure 6a–b, Figure 6 - figure supplement 1, and Video 4). Electrical coupling is the best candidate for rapid redistribution of a hyperpolarization current among B-type motor neurons (P*acr-5*::Arch). In both *unc-7* mutants and AVB-ablated worms, whole body paralysis could still be induced upon silencing mid-body and posterior B-type motor neurons (Figure 6c) using the maximum laser intensity, suggesting that the hyperpolarization signal could still be transduced in the absence of AVB-B gap junctions. In *unc-9* mutants, however, rhythmic bending in the anterior body persisted when mid-body B-type motor neurons were silenced (Figure 6a, 6c and Video 5). Restoring UNC-9 expression in cholinergic motor neurons, including the B- and A-type motor neurons (P*acr-2*::UNC-9), restored the ability to optogenetically induce whole body paralysis (Figure 6c). Therefore, electrical couplings among motor neurons contributed to the paralytic effect.

The probability for optogenetically inducing whole-body paralysis, however, was dose-dependent. When the mid-body B-type motor neurons were inactivated at lower laser intensity, which likely reduced the degree of hyperpolarization, forward locomotion was not abolished. Instead, both undulation amplitude and locomotor speed were reduced (Figure 6d–e). Interestingly, in the absence of AVB interneurons, a higher laser intensity was required to modify the locomotor kinematics and to induce whole worm paralysis (Figure 6d-e). These results suggest a potential mechanism by which gap junctions between motor neurons and AVB-B gap junctions function together to retrogradely

regulate head bending activity, and hence reconfigure the dynamics of worm body undulation.

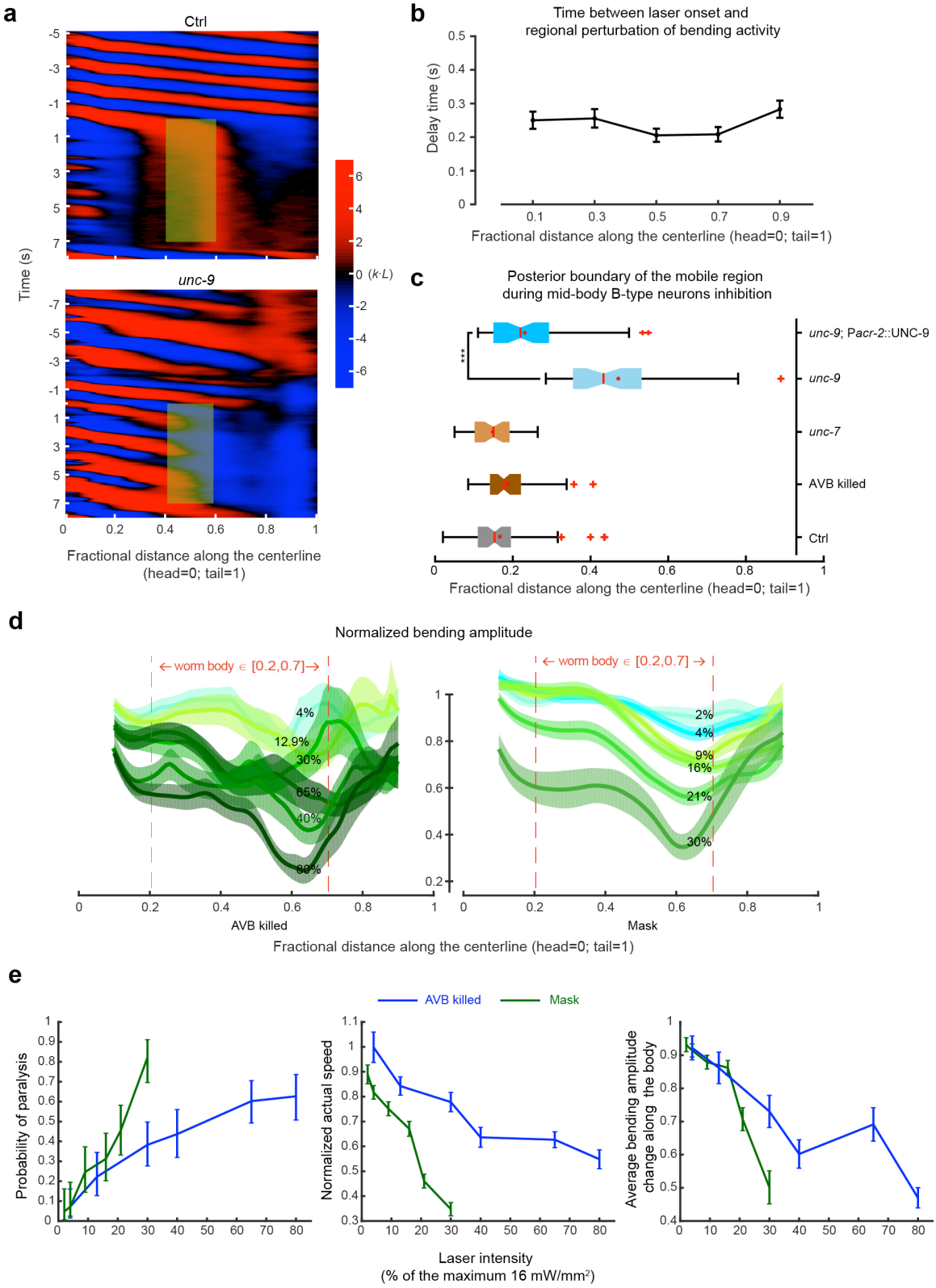

Figure 6 Electrical coupling among motor neurons and AVB-B gap junctions allows for rapid and reciprocal interactions between head and body motor activities. **(a)** Comparison of representative curvature kymographs of a control [P*acr-5*::Arch; P*unc-4*::TWK-18(gf)] and *unc-9* mutant [*unc-9*(*fc16*); P*acr-5*::Arch; P*unc-4*::TWK-18(gf)] worm during optogenetic inhibition of mid-body B-type motor neurons. Green shaded regions are selected regions (0.4–0.6 fractional distance) subjected to 0–7 s stimulation by the green laser. **(b)** Delay time between the onset of green laser and changes in bending. Error bars are s.e.m., also see Figure 6 - figure supplement 1. **(c)** Quantification of the whole-body paralytic effect during optogenetic inhibition of mid-body B-type motor neurons. Red crosses are outliers, red lines are medians, red dots are means, error bars represent Q1-1.5IQR and Q3+1.5IQR, respectively, and notches indicate 95% confidence interval. In *unc-9* mutants, the boundary shifted towards the mid-body, reflecting that the anterior body could still undulate. *** $p < 0.0001$ ($p = 2.4\times10^{-11}$), Mann-Whitney U test. Control [P*acr-5*::Arch; P*unc-4*::TWK-18(gf)], n = 70 measurements, 17 worms; *unc-7* [*unc-7*(*hp121*); P*acr-5*::Arch; P*unc-4*::TWK-18(gf)] n = 43 measurements, 11 worms; *unc-9* [*unc-9*(*fc16*); P*acr-5*::Arch; P*unc-4*::TWK-18(gf)] n = 59 measurements, 17 worms; AVB-ablated (P*lgc-55*::miniSOG, P*acr-5*::Arch) n = 65 measurements, 18 worms; UNC-9 rescued in the B-type and A-type motor neurons [*unc-9*(*fc16*); P*acr-5*::Arch; P*acr-2*::UNC-9] n = 48 measurements, 9 worms. **(d)** Laser intensity-dependent effects on the bending amplitude along the body. Error bars are s.e.m. **(e)** Laser intensity-dependent effects on efficacy for inducing whole-body paralysis, locomotion speed and mean amplitude decreases along the body [0.2, 0.7]. Error bars (speed and amplitude) are s.e.m., error bars (paralysis) are 95% binomial proportion confidence intervals. $n \geq 42$ measurements, ≥ 6 worms for each data point. Maximum laser intensity: 16 mW/mm^2.

Discussion

Electrical synapses are prevalent in invertebrate motor circuits, as well as in developing and mature vertebrate spinal cords [38-40]. The functional implications of gap junctions in the context of motor circuits and behavior can be counterintuitive, confounding, and are often underestimated [41, 42]. For example, in the mature zebrafish spinal cord, electrical couplings between motor neurons and premotor interneurons point to a nimble feedback mechanism for modulating rhythmic activity [43]. Experiments and modeling of crustacean stomatogastric ganglions suggest that the interplay between electrical and chemical synapses provides degenerate circuit mechanisms for switching between fast and slow oscillatory behaviors [44]. In the reversal motor circuit of *C. elegans*, the electrical coupling between AVA premotor interneurons and A-type motor neurons

provides state-dependent effects. At rest, they exhibit a shunting effect, by which the activity level in the backward locomotion circuit is suppressed so that a bias towards forward movement can be established [29]. Upon stimulation, these gap junctions allow antidromic-rectification of A-type motor neuron activity that prolongs reversal movement [45].

In the motor circuit that drives *C. elegans* forward movement, we discovered that AVB-B electrical couplings induced intrinsic oscillations in mid-body B-type motor neurons, and facilitated undulatory wave propagation. To better understand how descending inputs drove the bifurcation of motor neuron dynamics, we developed a nonlinear dynamic model based on voltage dependent conductance. Detailed characterization of the intrinsic membrane conductance and experimental test of our model required electrophysiological recordings in motor neurons, a difficult technique that has only recently become possible [45]. Intriguingly, a complementary study of the *C. elegans* reversal motor circuit found that voltage-dependent Ca^{2+} channels were required for generating intrinsic rhythmic activity in the A-type motor neurons (Shangbang Gao and Mei Zhen, personal communication, May 2017). Whether the same channels drive B-type motor neuron oscillation will be addressed in future studies.

Coordinated movement in larger animals involves networks of CPGs that are coupled through mechanosensory feedback [5]. In leech, stretch-sensitive feedback can alter the intersegmental phase lags between CPGs [10, 46]. During stick insect walking, proprioceptive feedback can entrain the motor patterns that drive individual joints, leading to interjoint coordination [13]. Specific classes of mechanosensory neurons in fly larvae are required for the propagation of peristaltic waves [47, 48].

Here, our data indicate that distributed CPGs, operated by at least some B-type motor neurons, exist in the *C. elegans* ventral nerve cord. Because worms must adapt to extreme ranges of external mechanical loads imposed by a changing environment [34], directional proprioceptive signals, also transduced by B-type motor neurons [30], are essential for entraining the rhythm of body oscillators, and for propagating coherent bending waves

from the head to the tail (Figure 7). In a linear coupling model where motor neurons passively respond to proprioceptive inputs, bending amplitude would suffer an exponential decay towards the tail. Our experimental finding and theoretical analysis thus provide new insight into the interplay between sensory feedback and intrinsic oscillators within the motor circuit.

We also found a previously unknown role of electrical couplings between motor neurons, which permits rapid and reciprocal interaction between the head and body motor activities (Figures 6–7). Over-expression of UNC-9 in the B-type motor neurons led to constitutive paralysis (Video 6); we suspect that strong electrical couplings between motor neurons tend to synchronize motor activity along the whole body, thus deteriorating bending wave propagation. Weak electrical couplings between motor neurons, on the other hand, might help mediate head bending activity and augment the excitability of motor neurons along the body. Direct testing of the functional contribution of local electrical couplings requires the elimination of electrical synapses between motor neurons, while sparing the AVB-B ones. Current genetic tools for manipulating gap junction expression with defined wiring specificity remain to be developed because both types of gap junctions require UNC-9 innexin.

UNC-9 hemichannels are also expressed by the body wall muscle cells [49]. Could electrical couplings between muscle cells and those between motor neurons have similar functions? We (and others) found that optogenetic inhibition of mid-body muscle cells did not affect bending activity in the anterior body region, but did abolish bending activity in the posterior body region [50], consistent with our proprioceptive coupling model (Figure 7). Furthermore, in *unc-13* mutants, where all chemical synaptic inputs from motor neurons to muscles are eliminated, targeted optogenetic activation of ventral or dorsal muscle cells induces local body bending, not bending in neighboring regions [30]. These data suggest that in *C. elegans* any electrical coupling between body wall muscle cells only plays a restricted role in local bending activity.

Despite substantial anatomical differences between the worm motor circuit and those in higher organisms, we identified converging principles that govern coordinated locomotion. By integrating global descending signals, biomechanical feedback, and neuromuscular dynamics, our findings and models represent a key step towards a full system model of animal locomotion.

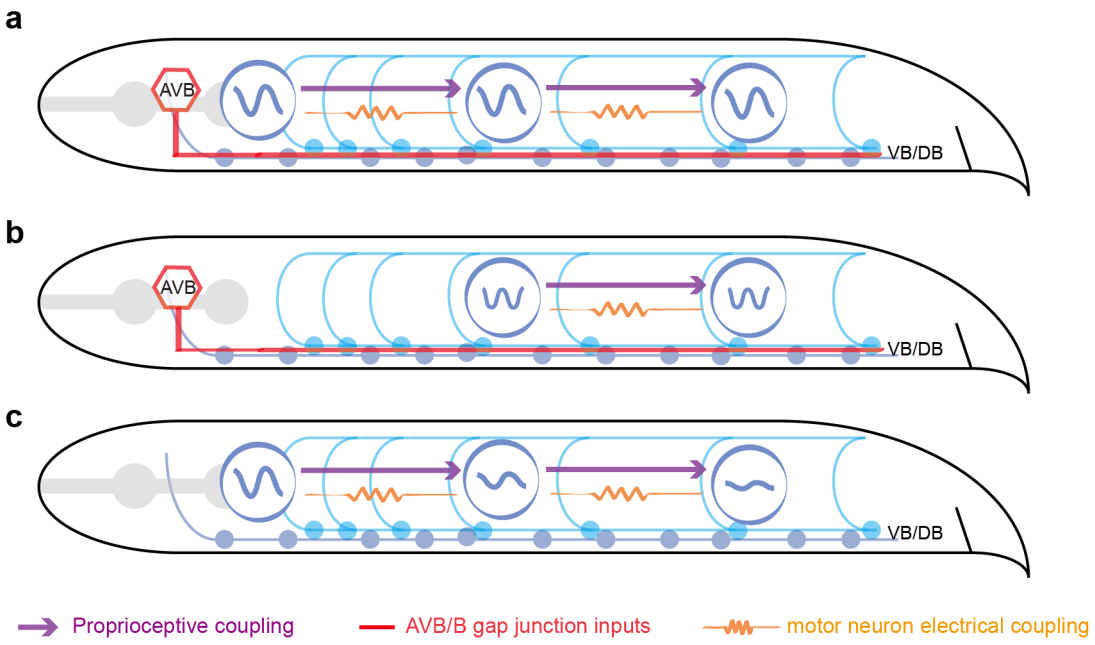

Figure 7 Model schematics of coordinating forward locomotion in *C. elegans*. **(a)** Proprioceptive coupling between B-type motor neurons, AVB-B gap junction coupling, and weak electrical coupling between motor neurons work synergistically to drive and propagate a coordinated undulatory wave from the head to the tail. **(b)** When a strong and time-varying proprioceptive signal from an anterior body region is absent, AVB-B gap junction coupling induces mid-body high frequency undulation. **(c)** In the absence of AVB-B gap junction inputs, proprioceptive couplings are less effective in propagating bending waves, leading to rapidly decaying bending amplitude towards the tail.

Methods

Worm strains and cultivation

Wild-type (N2), mutant, and transgenic worms were cultivated using standard methods [51]. Strain information can be found in the Supplementary Experimental Procedures. Transgenic worms used in all optogenetic experiments were cultivated in the dark at 20–25°C on NGM plates with *Escherichia coli* OP50 and all-*trans* retinal (ATR). We performed all experiments using young adult hermaphrodites.

Microfluidic device

Custom microfluidic devices were fabricated in polydimethylsiloxane (PDMS) using soft lithography. We loaded each microfluidic channel with dextran solution [~25% dextran in M9 buffer (1 Pa·s viscosity)]. An individual worm was transferred into the inlet of each microfluidic channel and worm position within each channel was manually controlled by syringes connected to polyethylene tubing.

Behavioral quantification and optogenetic manipulation

Experiments were performed on a Nikon inverted microscope (Ti-U, Japan) under 10× magnification with dark field illumination. Worms were immersed in viscous solution (~25% dextran in M9 buffer in most cases), sandwiched between two glass slides, and retained within the field of view of an imaging objective by a custom tracking system. Video sequences were taken by a Basler CMOS camera (aca2000-340km, Germany), and the worm body centerline was extracted in real time. We used MATLAB custom software (MathWorks, Inc. Natick, MA, USA) for post-processing behavioral data. We used the CoLBeRT system [50] to perform spatially-selective optogenetic manipulation for different motor circuit components. For optogenetic inhibition, we used a 561-nm solid-state laser with maximum intensity at 16 mW/mm^2.

In the relevant figure legends, the *n* numbers, in most cases, denote the numbers of measurements on indicated numbers of different animals for the experiments, and represent both independent biological replication and technical replication.

Optogenetic ablation

Optogenetic ablation was carried out using transgenic strains, in which mitochondrially targeted miniSOG (mini singlet oxygen generator) was specifically expressed in *C. elegans* neurons. Upon blue light illumination, mito-miniSOG caused rapid cell death in a cell-autonomous manner [33]. To ablate AVB neurons [*Plgc*-55(B)::miniSOG or *Psra-11*::miniSOG], L3/early L4 worms cultivated on OP50 were transplanted to an unseeded NGM plate, restricted within a 1.7 cm^2 area via filter paper with a hole in the center and soaked with 100 μM $CUCL_2$. Worms were illuminated with blue LED light (M470L3-C5, Thorlabs, Inc., USA) with an intensity of 80.2 mW/cm^2, measured by a power meter (PM16-130, Thorlabs, Inc., USA). The temporal sequence was 0.5/1.5 s on/off pulses for 30 min. After illumination, worms were transplanted to newly OP50-seeded NGM plates with/without ATR for behavioral experiments. Mask ablations were performed via green light illumination using the same genotype under otherwise the same experimental conditions.

For selective B-type motor neuron ablation (*Pacr-5*::miniSOG), single L3/early L4 worms were transferred from the OP50-seeded NGM plates to 3% agarose (wt/vol) coated glass slides. The worms were covered by a cover glass to remain stationary. Spatially selective illumination patterns were generated by a digital micromirror device (DLI4130 0.7 XGA, Digital Light Innovations, TX, USA) to target individual neurons through a 20× objective mounted on a Nikon inverted microscope (Ti-U, Japan). Neurons were identified using mCherry fluorescence signals. We used a 473-nm blue laser with an intensity of 29 mW/mm^2. The temporal sequence was 0.5/1.5 s on/off pulses for 15 min. After illumination, the worms were recovered by 2 μl of M9 buffer, and then transferred to OP50-seeded NGM plates with/without ATR for behavioral experiments.

Linear proprioceptive coupling model for undulatory wave propagation

We first developed a linear coupling model to simulate wave propagation along the body of *C. elegans*. In this model, the head motor circuit contains an oscillator that dominates the rhythmic motion of the whole body. Other segments cannot oscillate by themselves, but oscillate according to the proprioceptive input from the anterior segment. This simple

phenomenological model does not simulate the detailed dynamics of individual neurons, but instead aims to elucidate several key properties of wave propagation based on linear proprioceptive coupling.

The dynamics of the head oscillator are governed by the following equations:

$$\begin{cases} \tau_s \dfrac{dv}{dt} = v - \beta v^3 - \mathrm{a}k \\ \tau_h \dfrac{du}{dt} = -u + v \\ \tau_\eta \dfrac{dk}{dt} = -k + \alpha_{max} * u/b\,, \end{cases} \qquad \text{(Equation 5)}$$

where v describes the relative neural activity of the head motor neurons, a variable that represents the dorsal-ventral bias of neural activity. When dorsal head motor neurons have stronger neural activity than ventral ones, $v > 0$, and vice versa. The nonlinear term, $v - \beta v^3$, as well as the negative sensory feedback term $-\mathrm{a}k$ are critical for generating head oscillation. The second equation relates neural activity and muscle torque and the third equation relates muscle torque and body shape change in a defined segment. Their functional forms are identical to those in Equation 1. According to earlier work [30, 34], the time constant:

$$\tau_\eta = \frac{C_N}{b}\left(\frac{2\pi}{\lambda}\right)^4 \approx \frac{30\eta}{b}\left(\frac{2\pi}{\lambda}\right)^4, \qquad \text{(Equation 6)}$$

where C_N is the drag coefficient perpendicular to the worm body, a parameter that is proportional to the viscosity of medium η. In the regime of large viscosity, $\tau_\eta \gg \tau_h, \tau_\eta \gg \tau_s$, and the period of the oscillator is largely determined by τ_η.

Equation 5 allows for the generation of rhythmic head bending activity, and the oscillation frequency ($f \sim 1/\tau_\eta$) decreases with viscosity, a key phenomenon consistent with experimental observations (Figure 3c and [34]). Apart from the head, we divided the

worm body into five segments (the number of segments was not essential for our theoretical argument), each with different dynamics, as described in Equation 1. The combination of Equations 5 and 1 allows the propagation of the head bending activity along the whole worm body. Equations 5 and 1 arise naturally from a biologically more realistic model, where dorsal and ventral activities are treated separately. In this case, we have:

$$\begin{cases} \tau_s \dfrac{dv_d}{dt} = v_d - \beta {v_d}^3 - \mathrm{a}k \\ \tau_h \dfrac{du_d}{dt} = -u_d + v_d \\ \tau_s \dfrac{dv_v}{dt} = v_v - \beta {v_v}^3 + \mathrm{a}k \\ \tau_h \dfrac{du_v}{dt} = -u_v + v_v \\ \tau_\eta \dfrac{dk}{dt} = -k + \alpha_{max} * (u_d - u_v)/b \end{cases} \quad \text{Head} \qquad \text{(Equation 7)}$$

$$\begin{cases} C_m \dfrac{dv_{di}}{dt} = g_m(-v_{di} + ck_{i-1}) - g(v_{di} - v_{AVB}) \\ \tau_h \dfrac{du_{di}}{dt} = -u_{di} + v_{di} \\ C_m \dfrac{dv_{vi}}{dt} = g_m(-v_{vi} - ck_{i-1}) - g(v_{vi} - v_{AVB}) \\ \tau_h \dfrac{du_{vi}}{dt} = -u_{vi} + v_{vi} \\ \tau_\eta \dfrac{dk_i}{dt} = -k_i + \alpha_{max} * (u_{di} - u_{vi})/b \end{cases} \quad \text{body}, i = 2,3, \ldots \qquad \text{(Equation 8)}$$

Subscripts *d* and *v* denote dorsal and ventral sides, respectively. If we subtract "dorsal" equations from "ventral" equations, Equations 1 and 5 will be derived, provided we consider that dorsal and ventral motor activities are anti-phased, namely $v_d = -v_i$ and $v_{di} = -v_{vi}$. Simulation using Equations 7 and 8 did not show any essential difference compared with simulation using Equations 5 and 1.

The linear proprioceptive coupling model makes two predictions that can be tested experimentally. First, abolishing head motor activity should eliminate undulatory wave

propagation. However, when the head and body were decoupled in our experiments, we observed high frequency undulation emerging from the mid-body. Second, while simulation suggested AVB-B gap junction coupling would deteriorate the propagation of the bending amplitude (Figure 2d), our experimental data revealed the opposite. Therefore, we concluded that the linear coupling model was oversimplified.

Parameters used in simulation are:

$$\mathrm{a} = 0.385\ mm, \alpha_{max}/b = 2mm^{-1}, \beta = 1.$$

$$C_m = 4.5\ \mathrm{nF}, g_m = 100\ pS, c = 0.6\ mm, \tau_h = 75\ ms, \tau_s = 75\ ms$$

$$\tau_\eta = \frac{C_N}{b}\left(\frac{2\pi}{\lambda}\right)^4 \approx \frac{30\eta}{b}\left(\frac{2\pi}{\lambda}\right)^4, \quad b = 9.5\times10^{-14}\mathrm{N} * m^2, \lambda = 1\ mm.$$

$$\eta = 1\mathrm{Pa} * \mathrm{s}.$$

Analytical solution to linear proprioceptive coupling model

To gain a deeper insight into the bending amplitude decay during wave propagation (Figure 2d), we developed an analytical understanding for the linear coupling model by transforming Equation 1 into a continuous form.

The dynamic equations for bending wave propagation can now be rewritten by the following equations:

$$\begin{cases} C_m \dfrac{\partial v}{\partial t} = g_m(-v + ck(x-l)). \\ \tau_\eta \dfrac{\partial k}{\partial t} = -k + \alpha_{max} v/b\,. \end{cases} \qquad 0 < x < L \qquad \text{(Equation 9)}$$

In the first equation, $ck(x-l)$ describes how proprioceptive couplings drive the change in neural activity in motor neurons. l is the characteristic length of proprioceptive coupling from an anterior body region, and L is the length of the worm. The second equation relates the change of body shape with neural activity. For simplicity, we dropped the equation that relates neural activity and muscle torque in Equation 1. The delay time

between neural activity and muscle torque, characterized by τ_h, was absorbed by the time constant τ_η in Equation 9.

We assert a harmonic motion to describe the motor activity of the head. Thus, $v(x)$ and $k(x)$ can be written as:

$$\begin{cases} v = v_0 \exp\left(i\left(\frac{2\pi x}{\lambda} - \omega t\right)\right). \\ k = k_0 \exp\left(i\left(\frac{2\pi x}{\lambda} - \omega t\right)\right). \end{cases} \quad x \leq 0 \qquad \text{(Equation 10)}$$

The neural activity and curvature are not in-phase. Thus, the phase factors are absorbed into coefficients v_0 and k_0, which are all complex numbers.

The self-consistent solution for the motor activity along the body is sinusoidal, namely

$$\begin{cases} v = V(x) \exp\left(i\left(\frac{2\pi x}{\lambda} - \omega t\right)\right). \\ k = K(x) \exp\left(i\left(\frac{2\pi x}{\lambda} - \omega t\right)\right). \end{cases} \quad 0 < x < L \qquad \text{(Equation 11)}$$

Substituting Equation 11 into Equation 9 and defining $\tau_m = C_m/g_m$, we have

$$-i\omega\tau_m V(x) = -V(x) + c\exp\left(-i\frac{2\pi l}{\lambda}\right)K(x-l). \qquad \text{(Equation 12)}$$

$$-i\omega\tau_\eta K(x) = -K(x) + \alpha_{max}V(x)/b. \qquad \text{(Equation 13)}$$

Replacing $K(x-l)$ with $K(x) - K'(x)l + K''(x)l^2/2$, and using $l \ll \lambda$, we find

$$\frac{cl^2}{2}K''(x) - clK'(x) + \left((i\omega\tau_m - 1)(1 - i\omega\tau_\eta)b/\alpha_{max} + c\right)K(x) = 0$$

(Equation 14)

The solution is

$$K(x) = k_0 \exp\left(-\frac{B + \sqrt{B^2 - 4AC}}{2A} x\right), \qquad \text{(Equation 15)}$$

where

$$A = \frac{cl^2}{2}, \quad B = -cl, \quad C = (i\omega\tau_m - 1)(1 - i\omega\tau_\eta)b/\alpha_{max} + c$$

Thus, the decaying length constant satisfies

$$1/\xi = \mathrm{Re}\frac{B + \sqrt{B^2 - 4AC}}{2A}. \qquad \text{(Equation 16)}$$

Expanding it to power series of ω and only preserving lower order terms, we have

$$\xi = \frac{l}{1 - \frac{c\alpha_{max}}{b} + \omega^2\left(\frac{c\alpha_{max}(\tau_c^2 + \tau_\eta^2)}{2b} + \left(\frac{c\alpha_{max}}{b} - 1\right)\tau_m\tau_\eta\right)}. \quad \text{(Equation 17)}$$

The time constant τ_η increases with viscosity of medium η, and the decay length constant ξ decreases with η.

To the leading order, the decay length constant can be approximated as

$$\xi \approx \frac{l}{1 - \frac{c\alpha_{max}}{b}}. \qquad \text{(Equation 18)}$$

When we incorporate electrical couplings between AVB interneurons and B-type neurons into this model, the equations become

$$\begin{cases} \tau_m \dfrac{\partial v}{\partial t} = -v - gv/g_m + ck(x-l). \\ \tau_\eta \dfrac{\partial k}{\partial t} = -k + \alpha_{max} v/b\,. \end{cases} \quad 0 < x < L, \qquad \text{(Equation 19)}$$

where g is the gap junction conductance. In this case, the decay length constant reduces to:

$$\xi \approx \frac{l}{1 - \frac{g_m c \alpha_{max}}{(g+g_m)b}}, \qquad \text{(Equation 20)}$$

which further deteriorates the propagation of the bending amplitude. This prediction is inconsistent with our experimental observations.

Nonlinear proprioceptive coupling model

The discrepancy between our theoretical and experimental observations forced us to develop a modified nonlinear coupling model, with the head oscillator governed by the same dynamics as that in the linear coupling model:

$$\begin{cases} \tau_s \dfrac{dv_d}{dt} = v_d - \beta {v_d}^3 - \mathrm{a}k \\ \tau_h \dfrac{dn_d}{dt} = -n_d + v_d \\ \tau_s \dfrac{dv_v}{dt} = v_v - \beta {v_v}^3 + \mathrm{a}k \\ \tau_h \dfrac{dn_v}{dt} = -n_v + v_v \\ \tau_\eta \dfrac{dk}{dt} = -k + \alpha_{max} * (n_d - n_v)/b \end{cases} \qquad \text{(Equation 21)}$$

For all other segments, our model incorporated the experimental observations that B-type motor neurons generate intrinsic oscillations when the head and body are decoupled and when AVB interneurons and B-type motor neurons are electrically coupled ($g > 0$). The intrinsic membrane properties in the B-type motor neurons remain unknown. For

simplicity, we developed a phenomenological model based on active Ca^{2+} and K^{+} conductances [37].

The motor activity in a given body segment is now governed by the following equations:

$$\begin{cases} C_m \frac{dV_{di}}{dt} = -g_L(V_{di} - E_L) - g_{Ca} m_\infty(V_{di}) * (V_{di} - E_{Ca}) - g_K n_{di} * (V_{di} - E_K) + c' k_{i-1} + g(V_{AVB} - V_{di}) \\ \tau_n \frac{dn_{di}}{dt} = -n_{di} + n_\infty(V_{di}) \\ C_m \frac{dV_{vi}}{dt} = -g_L(V_{vi} - E_L) - g_{Ca} m(V_{vi}) * (V_{vi} - E_{Ca}) - g_K n_{vi} * (V_{vi} - E_K) - c' k_{i-1} + g(V_{AVB} - V_{vi}) \\ \tau_n \frac{dn_{vi}}{dt} = -n_{vi} + n_\infty(V_{vi}) \\ \tau_u \frac{dM_{di}}{dt} = -M_{di} + M(V_{di}) - M(V_{vi}) \\ \tau_u \frac{dM_{vi}}{dt} = -M_{vi} + M(V_{vi}) - M(V_{di}) \\ \tau_\eta \frac{dk_i}{dt} = -k_i + \alpha'_{max}/b * (M_{di} - M_{vi}) \end{cases}.$$

(Equation 22)

In Equation 22, m, n are voltage-dependent gating variables; $m_\infty(V), n_\infty(V)$ are steady-state activation functions. We assume that the time constant for the gating variable m is small and m follows instantaneously with the voltage. $M(V)$ relates cell membrane potential and muscle torque. We assume they all have sigmoidal functional forms:

$$m_\infty(V) = \frac{1}{1 + \exp\left(\frac{V - V_m}{\theta_m}\right)}, n_\infty(V) = \frac{1}{1 + \exp\left(\frac{V - V_n}{\theta_n}\right)}, M(V) = \frac{1}{1 + \exp\left(\frac{V - V_{mus}}{\theta_{mus}}\right)}.$$

(Equation 23)

$g(V_{AVB} - V)$ is the current flowing through the gap junction between AVB interneurons and B-type neurons, where V_{AVB} is the membrane potential of the AVB interneurons, held at a constant value.

The terms $-M(V_v)$ and $-M(V_d)$ in Equation 22 reflect contralateral inhibition from the D-type GABAergic motor neurons: dorsal D neurons can be activated by ventral B neurons and thereby inhibit dorsal muscle activity, and vice versa.

We simulated six segments (including the head), similar to that in the linear coupling model. The segment number was roughly in accordance with the number of DB-type motor neurons. The parameter values are listed below.

$$\tau_s = 50.0\,nF,\ \ \tau_h = 200\,ms,\ \ \ C_m = 3.0\,nF,\ \tau_n = 30\,ms, \tau_u = 85\,ms.$$

$$\tau_\eta = \frac{C_N}{b}(\frac{2\pi}{\lambda})^4 \approx \frac{30\eta}{b}\left(\frac{2\pi}{\lambda}\right)^4,\ \ \ b = 9.5\times10^{-14}\ \mathrm{N} * m^2, \lambda = 1\,mm.$$

$$g_m = 100\,pS, g_L = 100\,pS,\ \ g_{Ca} = 400\,pS, g_K = 500\,pS.$$

$$\mathrm{a} = 0.385\,mm, \beta = 1, \mathrm{c}' = \frac{5\mathrm{mA}}{\mathrm{mm}}, \frac{\alpha_{max}}{b} = 10\,mm^{-1}, \alpha'_{max}/b = 2.1\,mm^{-1}.$$

$$E_L = -60\,mV, E_{Ca} = 60\,mV, E_K = -70\,mV, E_0 = -60\,mV, V_{AVB} = -20\,mV.$$

$$V_m = -29\,mV, V_n = -55\,mV, V_{mus} = -45\,mV.$$

$$\theta_m = 10.25\,mV, \theta_n = 20\,mV, \theta_{mus} = 10\,mV.$$

$$\eta = 1\mathrm{Pa} * \mathrm{s}.$$

Comparing the case $g = 0$ and $g = 100\,pS$, we found that gap junction coupling between AVB interneurons and B-type neurons could equalize the bending amplitude (Figure 5c). High frequency oscillation within middle segments could also be generated when the head and body were decoupled (Figure 5a).

Acknowledgments

The authors thank Christopher Fang-Yen and Anthony Fouad for helpful discussion. This work was funded by the CAS Hundred Talents Plan and the National Science Foundation of China (NSFC-31471051 and NSFC-91632102 to Q. Wen) and the Canadian Institute of Health Research (CIHR-MOP93619, MOP123250 to M. Zhen).

Competing Interests

The authors declare no competing financial interests.

References

1. Brown, T.G., *The Intrinsic Factors in the Act of Progression in the Mammal.* Proceedings of the Royal Society of London Series B-Biological Sciences, 1911. **84**(572): p. 308-319.
2. Delcomyn, F., *Neural basis of rhythmic behavior in animals.* Science, 1980. **210**(4469): p. 492-8.
3. Grillner, S., *The motor infrastructure: from ion channels to neuronal networks.* Nat Rev Neurosci, 2003. **4**(7): p. 573-86.
4. Kiehn, O., *Locomotor circuits in the mammalian spinal cord.* Annu Rev Neurosci, 2006. **29**: p. 279-306.
5. Marder, E., et al., *Invertebrate central pattern generation moves along.* Curr Biol, 2005. **15**(17): p. R685-99.
6. Marder, E. and R.L. Calabrese, *Principles of rhythmic motor pattern generation.* Physiological Reviews, 1996. **76**(3): p. 687-717.
7. Mullins, O.J., et al., *Neuronal control of swimming behavior: comparison of vertebrate and invertebrate model systems.* Prog Neurobiol, 2011. **93**(2): p. 244-69.
8. Pearson, K.G., *Proprioceptive regulation of locomotion.* Curr Opin Neurobiol, 1995. **5**(6): p. 786-91.
9. McClellan, A.D. and W. Jang, *Mechanosensory inputs to the central pattern generators for locomotion in the lamprey spinal cord: resetting, entrainment, and computer modeling.* J Neurophysiol, 1993. **70**(6): p. 2442-54.
10. Yu, X. and W.O. Friesen, *Entrainment of leech swimming activity by the ventral stretch receptor.* J Comp Physiol A Neuroethol Sens Neural Behav Physiol, 2004. **190**(11): p. 939-49.
11. Pearson, K.G., *Generating the walking gait: role of sensory feedback.* Prog Brain Res, 2004. **143**: p. 123-9.
12. Akay, T., et al., *Degradation of mouse locomotor pattern in the absence of proprioceptive sensory feedback.* Proc Natl Acad Sci U S A, 2014. **111**(47): p. 16877-82.
13. Hess, D. and A. Buschges, *Role of proprioceptive signals from an insect femur-tibia joint in patterning motoneuronal activity of an adjacent leg joint.* J Neurophysiol, 1999. **81**(4): p. 1856-65.
14. Woo, S.H., et al., *Piezo2 is the principal mechanotransduction channel for proprioception.* Nature Neuroscience, 2015. **18**(12): p. 1756-1762.
15. Lemon, R.N., *Descending pathways in motor control.* Annu Rev Neurosci, 2008. **31**: p. 195-218.
16. Hagglund, M., et al., *Activation of groups of excitatory neurons in the mammalian spinal cord or hindbrain evokes locomotion.* Nat Neurosci, 2010. **13**(2): p. 246-52.
17. Thiele, T.R., J.C. Donovan, and H. Baier, *Descending control of swim posture by a midbrain nucleus in zebrafish.* Neuron, 2014. **83**(3): p. 679-91.
18. Severi, K.E., et al., *Neural control and modulation of swimming speed in the larval zebrafish.* Neuron, 2014. **83**(3): p. 692-707.
19. Buchanan, J.T., et al., *Reticulospinal Neurons Activate Excitatory Amino-Acid Receptors.* Brain Research, 1987. **408**(1-2): p. 321-325.

20. Bouvier, J., et al., *Descending Command Neurons in the Brainstem that Halt Locomotion.* Cell, 2015. **163**(5): p. 1191-203.
21. Esposito, M.S., P. Capelli, and S. Arber, *Brainstem nucleus MdV mediates skilled forelimb motor tasks.* Nature, 2014. **508**(7496): p. 351-6.
22. Weeks, J.C. and W.B. Kristan, *Initiation, Maintenance and Modulation of Swimming in the Medicinal Leech by the Activity of a Single Neuron.* Journal of Experimental Biology, 1978. **77**(Dec): p. 71-88.
23. Friesen, W.O. and W.B. Kristan, *Leech locomotion: swimming, crawling, and decisions.* Curr Opin Neurobiol, 2007. **17**(6): p. 704-11.
24. Dickinson, M.H., et al., *How animals move: An integrative view.* Science, 2000. **288**(5463): p. 100-106.
25. Chen, B.L., D.H. Hall, and D.B. Chklovskii, *Wiring optimization can relate neuronal structure and function.* Proceedings of the National Academy of Sciences of the United States of America, 2006. **103**(12): p. 4723-4728.
26. White, J.G., et al., *The Structure of the Nervous-System of the Nematode Caenorhabditis-Elegans.* Philosophical Transactions of the Royal Society of London Series B-Biological Sciences, 1986. **314**(1165): p. 1-340.
27. White, J.G., et al., *The structure of the ventral nerve cord of Caenorhabditis elegans.* Philos Trans R Soc Lond B Biol Sci, 1976. **275**(938): p. 327-48.
28. Starich, T.A., et al., *Interactions between innexins UNC-7 and UNC-9 mediate electrical synapse specificity in the Caenorhabditis elegans locomotory nervous system.* Neural Development, 2009. **4**.
29. Kawano, T., et al., *An Imbalancing Act: Gap Junctions Reduce the Backward Motor Circuit Activity to Bias C. elegans for Forward Locomotion.* Neuron, 2011. **72**(4): p. 572-86.
30. Wen, Q., et al., *Proprioceptive coupling within motor neurons drives C. elegans forward locomotion.* Neuron, 2012. **76**(4): p. 750-61.
31. Zhen, M. and A.D. Samuel, *C. elegans locomotion: small circuits, complex functions.* Curr Opin Neurobiol, 2015. **33**: p. 117-26.
32. Altun, Z.F., et al., *High resolution map of caenorhabditis elegans gap junction proteins.* Dev Dyn, 2015. **244**(7): p. 903.
33. Qi, Y.B., et al., *Photo-inducible cell ablation in Caenorhabditis elegans using the genetically encoded singlet oxygen generating protein miniSOG.* Proc Natl Acad Sci U S A, 2012. **109**(19): p. 7499-504.
34. Fang-Yen, C., et al., *Biomechanical analysis of gait adaptation in the nematode Caenorhabditis elegans.* Proc Natl Acad Sci U S A, 2010. **107**(47): p. 20323-8.
35. Faumont, S., et al., *An image-free opto-mechanical system for creating virtual environments and imaging neuronal activity in freely moving Caenorhabditis elegans.* PLoS One, 2011. **6**(9): p. e24666.
36. Laurent, P., et al., *Decoding a neural circuit controlling global animal state in C. elegans.* Elife, 2015. **4**.
37. Izhikevich, E.M., *Dynamical systems in neuroscience : the geometry of excitability and bursting*. Computational neuroscience. 2007, Cambridge, Mass.: MIT Press. xvi, 441 p.
38. Connors, B.W. and M.A. Long, *Electrical synapses in the mammalian brain.* Annu Rev Neurosci, 2004. **27**: p. 393-418.

39. Kiehn, O. and M.C. Tresch, *Gap junctions and motor behavior.* Trends Neurosci, 2002. **25**(2): p. 108-15.
40. Szczupak, L., *Functional contributions of electrical synapses in sensory and motor networks.* Curr Opin Neurobiol, 2016. **41**: p. 99-105.
41. Manor, Y., et al., *Low-amplitude oscillations in the inferior olive: a model based on electrical coupling of neurons with heterogeneous channel densities.* J Neurophysiol, 1997. **77**(5): p. 2736-52.
42. Marder, E., *Electrical synapses: beyond speed and synchrony to computation.* Curr Biol, 1998. **8**(22): p. R795-7.
43. Song, J., et al., *Motor neurons control locomotor circuit function retrogradely via gap junctions.* Nature, 2016. **529**(7586): p. 399-402.
44. Gutierrez, G.J., T. O'Leary, and E. Marder, *Multiple mechanisms switch an electrically coupled, synaptically inhibited neuron between competing rhythmic oscillators.* Neuron, 2013. **77**(5): p. 845-58.
45. Liu, P., et al., *Antidromic-rectifying gap junctions amplify chemical transmission at functionally mixed electrical-chemical synapses.* Nat Commun, 2017. **8**: p. 14818.
46. Yu, X.T., B. Nguyen, and W.O. Friesen, *Sensory feedback can coordinate the swimming activity of the leech.* Journal of Neuroscience, 1999. **19**(11): p. 4634-4643.
47. Cheng, L.E., et al., *The role of the TRP channel NompC in Drosophila larval and adult locomotion.* Neuron, 2010. **67**(3): p. 373-80.
48. Guo, Y., et al., *Transmembrane channel-like (tmc) gene regulates Drosophila larval locomotion.* Proc Natl Acad Sci U S A, 2016. **113**(26): p. 7243-8.
49. Liu, Q., et al., *Low conductance gap junctions mediate specific electrical coupling in body-wall muscle cells of Caenorhabditis elegans.* J Biol Chem, 2006. **281**(12): p. 7881-9.
50. Leifer, A.M., et al., *Optogenetic manipulation of neural activity in freely moving Caenorhabditis elegans.* Nature Methods, 2011. **in press**.
51. Brenner, S., *The genetics of Caenorhabditis elegans.* Genetics, 1974. **77**(1): p. 71-94.

Videos

Video 1 | An *unc-7* mutant animal swam freely in solution at ~ 1 Pa·s viscosity. Despite anterior body undulation, the animal exhibited dragging in the tail.

Video 2 | Optogenetic inhibition of the anterior region of a freely swimming wild type worm induced high frequency undulation in the posterior body region.

Video 3 | A worm with UNC-7 expression restored in AVB and other neurons (P*sra-11*::UNC-7) swam in solution at ~ 1 Pa·s viscosity. Both bending amplitude and high-frequency undulation in the posterior body region were restored.

Video 4 | Optogenetic inhibition of the mid-body B-type motor neurons in a wild type worm resulted in whole body paralysis.

Video 5 | Optogenetic inhibition of the mid-body B-type motor neurons in an *unc-9* mutant worm led to paralysis in the posterior region, whereas the anterior body undulation persisted.

Video 6 | Over-expression of UNC-9 innexin in B-type motor neurons (P*acr-5*::UNC-9) caused whole body paralysis. Worms were incapable of propagating body undulations along their bodies.

Video 7 | Optogenetic activation of AVB premotor interneurons (P*sra-11*::Chrimson) could trigger forward locomotion from the pause state.

Figure 1 – supplement figure 1 | AVB-B electrical couplings facilitate undulatory wave propagation during forward locomotion

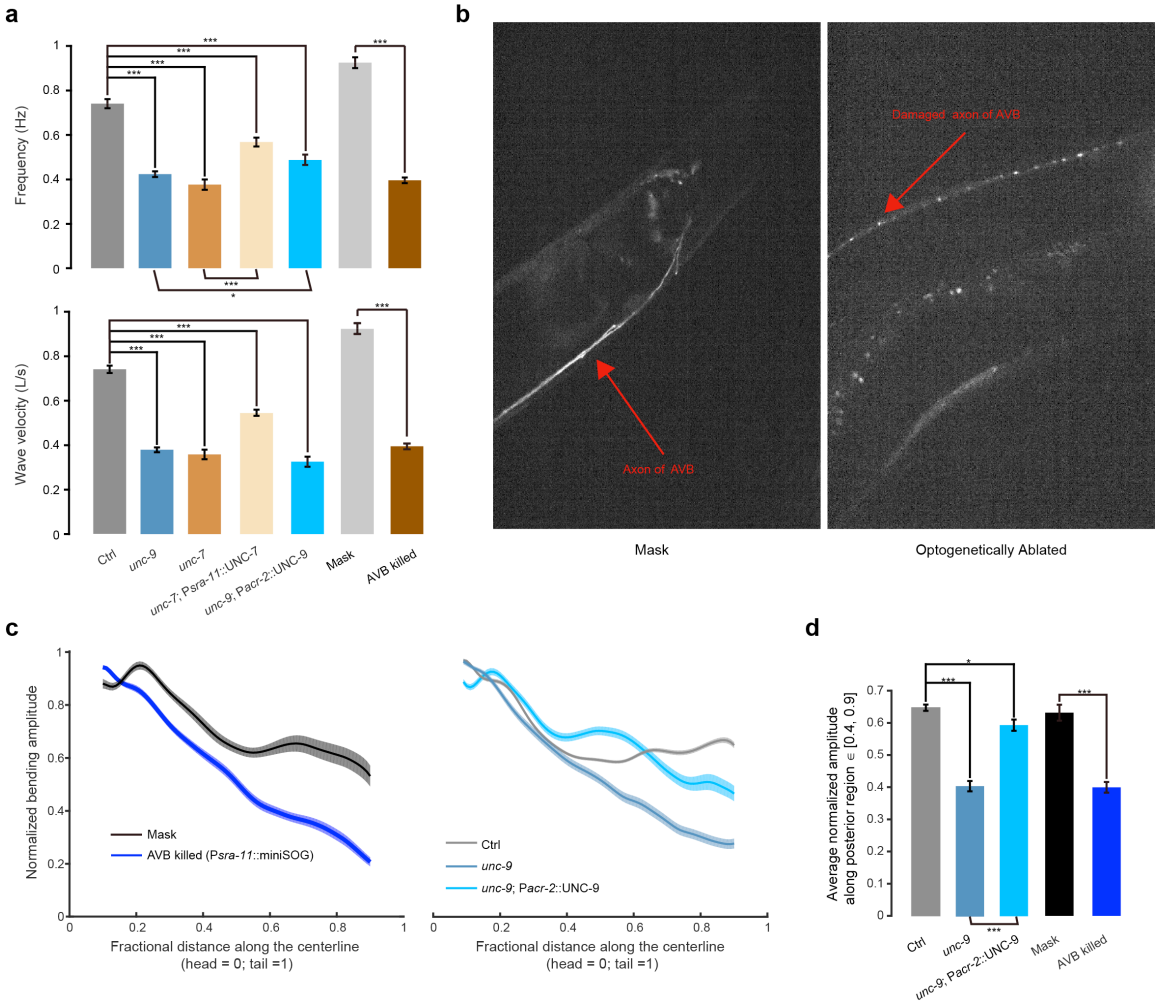

(a) Locomotion kinematics of tested strains. Upper panel shows the comparison of undulation frequency in viscous medium (~ 1 Pa·s). Lower panel shows the comparison of wave velocity, calculated in worm body length per second (*L*/*s*). Error bars show s.e.m. *** $p < 0.0001$, * $p = 0.01$ (Up: Ctrl and *unc-9* $p = 4.1\times10^{-28}$; Ctrl and *unc-7* $p = 1.7\times10^{-24}$; Ctrl and *unc-7;*P*sra-11*::UNC-7 $p = 8.8\times10^{-9}$; Ctrl and *unc-9;* P*acr-2*::UNC-9 $p = 1.13\times10^{-13}$; *unc-7;*P*sra-11*::UNC-7 and *unc-7* $p = 2.8\times10^{-9}$; Mask and AVB killed $p = 2.4\times10^{-39}$. Bottom: Ctrl and *unc-9* $p = 2.2\times10^{-33}$; Ctrl and *unc-7* $p = 3.1\times10^{-30}$; Ctrl and *unc-7;*P*sra-11*::UNC-7 $p = 1.9\times10^{-16}$; Ctrl and *unc-9;*P*acr-2*::UNC-9 $p = 2.7\times10^{-28}$; *unc-7;*P*sra-11*::UNC-7 and *unc-7* $p = 3.0\times10^{-10}$; *unc-9;*P*acr-2*::UNC-9 and *unc-9* $p = 0.01$; Mask and AVB killed $p = 5.6\times10^{-41}$), two-sample *t*-test with Bonferroni correction. Ctrl

[N2; P*acr-5*::Arch; P*unc-4*::TWK-18(gf)], n = 107 measurements, 13 worms; *unc-7* mutant, [*unc-7*(*hp121*); P*acr-5::*Arch; P*unc-4*::TWK-18(gf)], n = 99 measurements, 22 worms; *unc-9* mutant [*unc-9*(*fc16*); P*acr-5*::Arch; P*unc-4::*TWK-18(gf)], n = 144 measurements, 17 worms; AVB ablated worm [P*glc-55(*B*)*::tom20::miniSOG::UrSL::wCherry], n = 80 measurements, 13 worms; Mask, n = 96 measurements, 12 worms. **(b)** Comparison of AVB axon fluorescence signals in mask and AVB-ablated worms. Arrows indicate intact and damaged axons. **(c)** Left: Comparison of normalized bending amplitude along the worm body in mask and AVB-ablated worms. We used a different transgenic strain (P*sra-11*::miniSOG) to drive the expression of miniSOG in AVB neurons. Right: Comparison of normalized bending amplitude along the worm body in CTRL, *unc-9*, and UNC-9 rescue in B-type and A-type motor neurons [*unc-9*(*fc16*); P*acr-2*::UNC-9; P*acr-5*::arch]. Rescue of UNC-9 in B-type and A-type motor neurons largely restored the posterior bending amplitude. Shaded regions show s.e.m. **(d)** Bending amplitude averaged over the posterior region $\in$ [40, 90] of the worm body. ***$p < 0.0001$, *$p = 0.003$ (Ctrl and *unc-9* $p = 3.5\times10^{-23}$; *unc-9;*P*acr-2*::UNC-9 and *unc-9* $p = 1.7\times10^{-12}$; Mask and AVB killed $p = 2.4\times10^{-10}$), two-sample *t*-test with Bonferroni correction. Error bars represent s.e.m. Ctrl, n = 105 measurements, 13 worms; *unc-9* mutant, n = 93 measurements, 17 worms; UNC-9 rescue in motor neurons, n = 64 measurements, 9 worms. Mask, n = 28 measurements, 5 worms; AVB-ablated worms (P*sra-11*::tomm20::miniSOG) n = 100 measurements, 10 worms.

Figure 2 – supplement figure 1 | AVB-B electrical couplings are not necessary for transducing proprioceptive signals.

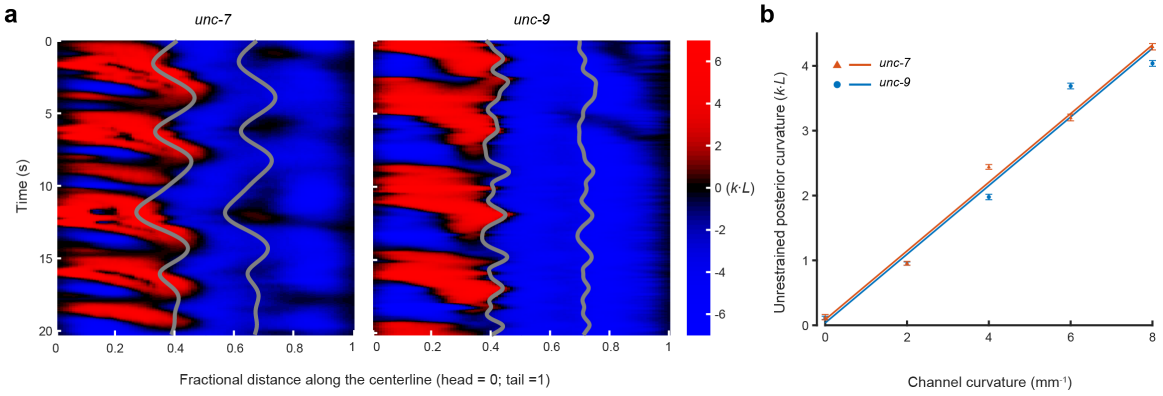

(a) Representative kymographs showing an *unc-7* mutant [*unc-7*(hp121); P*unc-4::*TWK-18(gf)] and an *unc-9* mutant worm [*unc-9*(fc16); P*unc-4::*TWK-18(gf)], whose mid-bodies were constrained in a microfluidic channel with defined curvature (6 mm^{-1}). Gray lines indicate anterior and posterior boundaries of the channel. **(b)** Unconstrained posterior body curvature as a function of channel curvature. Each data point: n = 5 worms, error bars represent s.e.m. Blue and red lines are linear fit ($R^2 > 0.97$).

Figure 3 – supplement figure 1 | Mid-body B motor neurons intrinsically generate rhythmic activity.

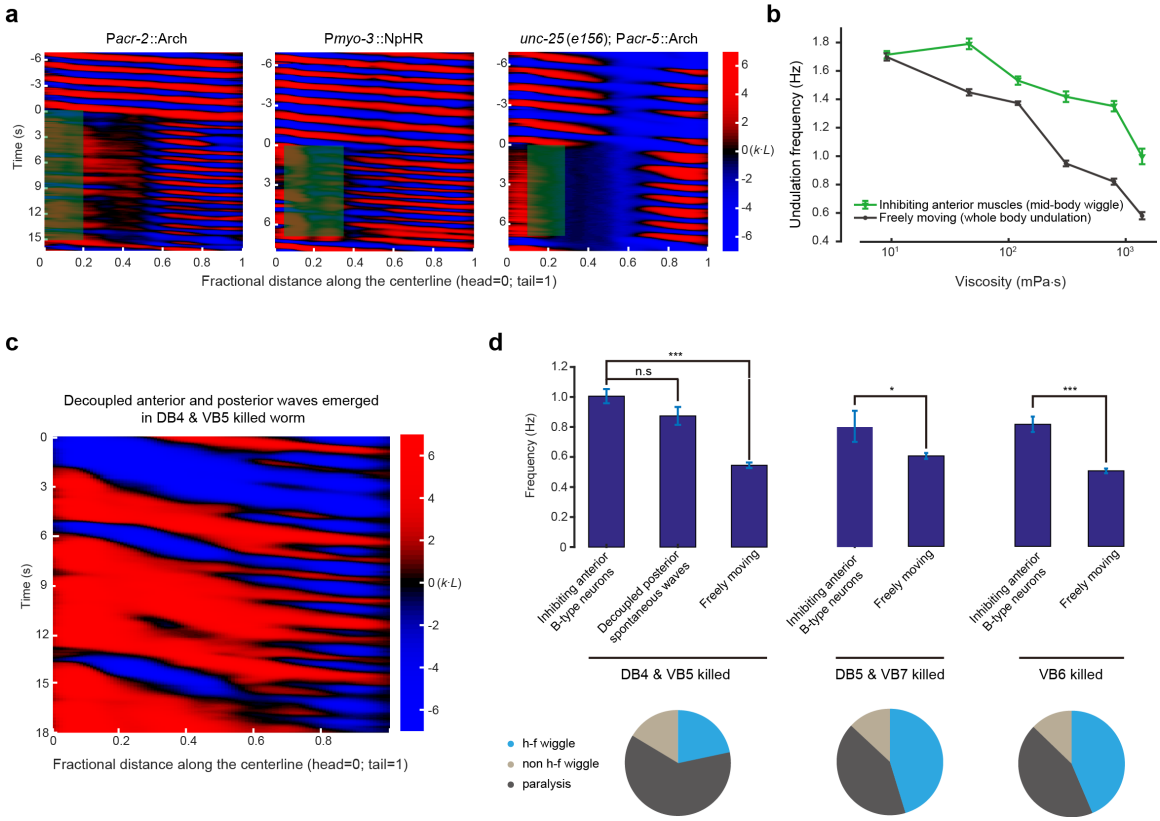

(a) Representative kymographs demonstrate that fast mid/posterior body undulatory waves could be induced by inhibiting anterior A- & B-type motor neurons (P*acr-2*::Arch, 11 out of 25 measurements) by inhibiting anterior muscle cells (P*myo-3*::NpHR, 52 out of 87 measurements) or by inhibiting anterior B-type motor neurons in GABA neurotransmitter-deficient worms [*unc-25*(e156); P*acr-5*::Arch, 33 out of 45 measurements]. **(b)** Undulation frequency with medium viscosity. Black, normal swimming worm; green, mid-body undulation when the head and body were decoupled by inhibiting anterior muscle cells. Each data point represents mean and s.e.m from $n \geq 4$ worms. **(c)** Representative kymographs of a freely swimming worm in which DB4 & VB5 motor neurons were optogenetically ablated (P*acr-5*::tomm20::miniSOG). Decoupled spontaneous waves emerged from anterior and posterior body regions. **(d)** Up, summary of undulation frequencies after selectively ablating a subset of B-type motor

neurons in the mid-body. Three behavioral outcomes were compared. (1) Fast mid-body undulation induced by optogenetically inhibiting anterior B-type motor neurons. (2) Spontaneous posterior bending waves in DB4&VB5-ablated worms. (3) Freely swimming worms. Bottom, pie chart summarizes worm locomotor states across trials during optogenetic inhibition of anterior B-type motor neurons. State definitions can be found in the main text. Error bars show s.e.m., *** $p < 0.0001$, n.s. $p = 0.15$ (DB4 & VB5 killed $p = 6.1\times10^{-13}$; DB5 & VB7 killed $p = 0.01$; VB6 killed $p = 5.8\times10^{-6}$), two-sample *t*-test. DB4 & VB5 killed $n = 11$ worms, DB5 & VB7 killed $n = 8$ worms, VB6 killed $n = 9$ worms.

Figure 4 – supplement figure 1 | AVB-B electrical couplings drive a bifurcation in B-type neuron dynamics

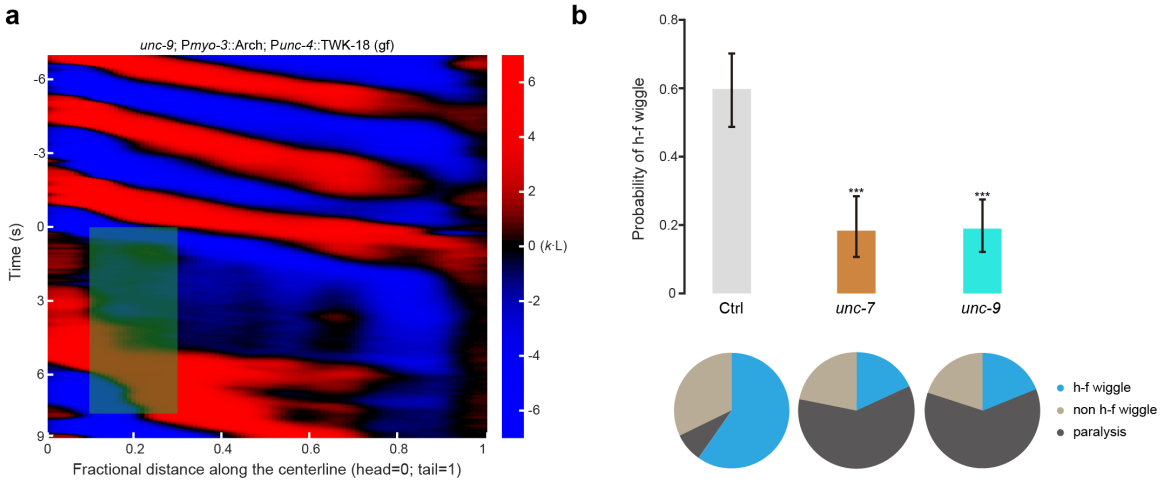

(a) Representative curvature kymographs of head-body-decoupled experiments in AVB-B gap junction-deficient *unc-9* mutants [*unc-9*; P*myo-3*::Arch; P*unc-4*::TWK-18(gf)]. Anterior muscle cells were optogenetically inhibited to abolish the proprioceptive signals arising from head bending activity. **(b)** Probability for inducing high frequency mid-body undulation when the head and body were decoupled by inhibiting anterior muscle cells. Pie chart summarizes worm locomotor states across trials. Error bars indicate 95% binomial proportion confidence interval. *** $p < 0.0001$ (Ctrl and *unc-7* $p = 3.6\times10^{-8}$; Ctrl and *unc-9* $p = 3.3\times10^{-9}$), Chi-Square test. Ctrl [P*myo*-3::NpHR, P*unc-4::*TWK-18(gf)], $n = 87$ measurements, 10 worms. *unc-7* mutant [*unc-7(hp121);* P*myo*-3::Arch*; Punc-4::*TWK-18(gf)], $n = 82$ measurements, 18 worms. *unc-9* mutant [*unc-9(fc16);* P*myo*-3::Arch*; Punc-4::*TWK-18(gf)], $n = 111$ measurements, 21 worms.

Figure 6 – supplement figure 1 | Electrical couplings between motor neurons allow for rapid and reciprocal interactions between head and body motor activities.

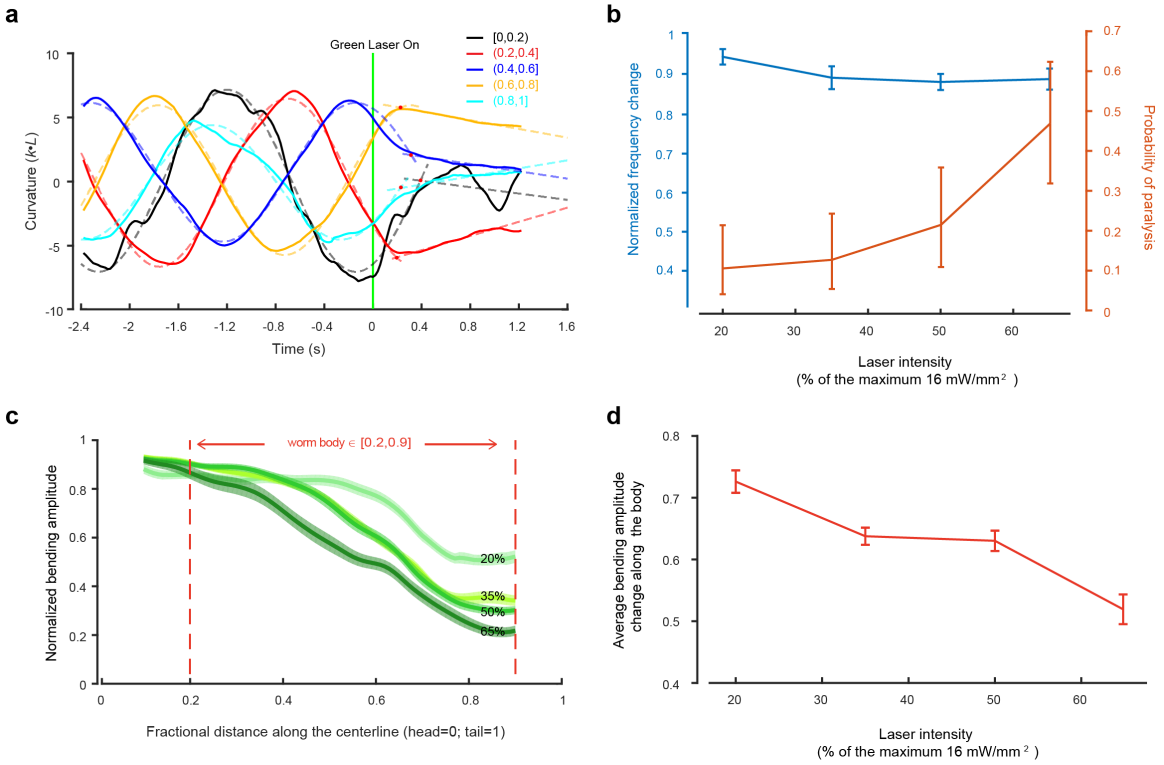

(a) Estimation of reaction time when mid-body B-type motor neurons were optogenetically inhibited. First, we fit the regional curvature with a sinusoidal function right before the green laser was turned on. Second, we performed a linear fit of regional curvature during the optogenetic inhibition. The crossover point (red dot) represents the wiggle-to-paralysis transition for each segment. Curvatures were averaged over a defined color-coded region, represented by a fractional distance along the worm body coordinates (head = 0, tail = 1). **(b)** Dose-dependent effect on the undulation frequency and efficacy for inducing whole-body paralysis when B-type motor neurons within a posterior body region (∈ [0.7, 0.9]) were optogenetically inhibited. Error bars (blue), s.e.m; error bars (orange), 95% binomial proportion confidence interval. $n \geq 5$ worms for each data point. **(c)** Dose dependent effect on the bending amplitude along the worm body when B-type motor neurons within a posterior body region (∈ [0.7, 0.9]) were optogenetically

inhibited. Shaded regions are s.e.m. **(d)** Average bending amplitude change along the body ∈ [0.2, 0.9]. Error bars are s.e.m. Maximum laser intensity was 16 mW/mm^2.

1 **Supplementary Table | Strain information**

2

3

Strain Name	Experiment	Genotype	Construct (plasmid no.); injection concentrations
WEN0315	B motor neuron inhibition in WT	*wenIs0001; wenEx0315*	P*acr-5*::Arch::UrSL::wCherry (pJH2918);P*odr-1*::gfp (wenIs0001) P*unc-4*::TWK::18(gf)::UrSL::wCherry (pJH2108) 30 ng/µL; P*lin-14*::gfp 20 ng/µL; P*myo-3*::wCherry (pJH1774) 2.5 ng/µL (wenEx0315)
WEN0317	B motor neuron inhibition in *unc-7* mutants; Microfluidic experiments	*wenIs0001; wenEx0317; unc-7*(*hp121*)	P*acr-5*::Arch:: UrSL::wCherry (pJH2918); P*odr-1*::gfp (WenIs0001) P*unc-4*::TWK::18(gf)::UrSL::wCherry (pJH2108) 30 ng/µL; P*lin-14*::gfp 20 ng/µL;P*myo-3*::wCherry (pjH1774) 2.5 ng/µL (wenEx0317)
WEN0304	B motor neuron inhibition in *unc-9* mutants; Microfluidic experiments	*wenEx0304; hpEx2088; unc-9*(*fc16*)	P*acr-5*::Arch:: UrSL::wCherry (pJH2918) 30 ng/µL; P*lin-14*::gfp 20 ng/µL (Wen Ex0304) P*unc-4*::TWK::18(gf)::UrSL::wCherry (pJH2108) ; P*odr-1*::gfp (hpEx2088)
ZM7297	AVB ablation	*hpIs331*;	P*lgc-55*(B)::tomm-20::miniSOG::UrSL::wCherry (pJH2890); lin-15
WEN0318	B motor neuron inhibition upon AVB ablation; Microfluidic experiments	*wenIs0001; hpIs331;*	P*acr-5*::Arch::UrSL::wCherry (pJH2918);P*odr-1*::gfp (wenIs0001) P*lgc-55*(B)::tomm-20::miniSOG::UrSL::wCherry (pJH2890) (hpIs331)
WEN0335	B motor neuron inhibition in *unc-7* mutants, with UNC-7 expression restored in AVB	*wenEx0335; wenIs0001; unc-7*(*hp121*)	P*unc-4*::TWK::18(gf)::UrSL::wCherry (pJH2108) 30 ng/µL; P*sra-11*::UNC-7(cDNA)::wCherry (pJH2037) 20 ng/µL; P*lin-14*::gfp 20ng/µL; P*myo-3*::wCherry 2.5 ng/µL (wenEx0335) P*acr-5*::Arch:: UrSL::wCherry (pJH2918); P*odr-1*::gfp (wenIs0001)
WEN0314	B motor neuron ablation; Microfluidic experiments	*wenIs0001; hpIs374;*	P*acr-5*::Arch:: UrSL::wCherry (pJH2918); P*odr-1*::gfp (hpIs374) P*acr-5*::tomm-20::miniSOG::UrSL::wCherry (pJH2842) (wenIs0001)
WEN0001	B motor neuron inhibition	*wenIs0001*	P*acr-5*::Arch::UrSL::wCherry (pJH2918); P*odr-1*::gfp (wenIs0001)
WEN0320	B motor neuron inhibition upon AVB ablation	*wenIs0001; wenEx0320*	P*acr-5*::Arch::UrSL::wCherry (pJH2918); P*odr-1*::gfp (wenIs0001) P*sra-11*::tomm-20::miniSOG::UrSL::wCherry (quan0065) 50 ng/µL; P*myo-3*::wCherry 2.5 ng/µL (wenEx0320)
ZM9275	A & B motor neuron inhibition	*hpIs615*	P*acr-2*(s)::Arch::wCherry (pJH3717) (hpIs615)
ZX444.6	Muscle inhibition	*zxEx29; lin-15*(*n765ts*)	Pmyo-3::NpHR::ECFP; lin-15+ (zxEx29)
WEN0307	B motor neuron inhibition in *GABA* deficient mutants	*wenIs0001*; *unc-25*(*e156*)	P*acr-5*::Arch::UrSL::wCherry (pJH2918); P*odr-1*::gfp (wenIs0001)
ZM7796	B motor neuron ablation	*hpIs374*	P*acr-5*::tomm-20::miniSOG::UrSL::wCherry (pJH2842) (hpIs374)
WEN0372	AVB activation	*wenEx*0372	P*sra-11*::Chrimson::wCherry (quan0164) 30 ng/µl; P*lin-24*::GFP (wenEx0372)
WEN0363	Muscle	*wenEX*0363;	P*myo-3*::Arch::UrSL::wCherry (quan0124) 30 ng/µl;

	inhibition in *unc-7* mutants	*unc-7*(*hp121*)	P*unc-4*::TWK-18(gf)::UrSL::wCherry (pJH2108) 30 ng/µl (wenEx0363)
WEN0323	Muscle inhibition in *unc-9* mutants	*wenEx0323*; *unc-9*(*fc16*)	P*myo-3*::Arch::UrSL::wCherry (quan0124) 30 ng/µl; P*unc-4*::TWK-18(gf)::UrSL::wCherry (pJH2108) 30 ng/µl (wenEx0323)
WEN0337	*unc-9* mutants with restored expression in A and B motor neurons	*wenEx0337; unc-9*(*fc16*)	P*acr-2*::UNC-9::wCherry (pJH1897) 2 ng/µl; P*acr-5*::Arch:: UrSL::wCherry (pJH2918) 30 ng/µl (wenEx0337)
WEN0366	Overexpression of UNC-9 in B motor neurons	*wenEx0366*	P*acr-5*::Arch:: UrSL::wCherry (pJH2918) 30 ng/µl; P*acr-5*::UNC-9 (pJH2140) 30 ng/µl (wenEx0366)

1